Fundamental Understanding of Material Extrusion Additive Manufacturing

Franck Pigeonneau, D. Xu, Jean-François Agassant

Fundamental understanding of material extrusion additive manufacturing

F. Pigeonneau*, D. Xu, J.-F. Agassant

MINES Paris, PSL University, Centre for Material Forming, CNRS UMR 7635, CS 10207, rue Claude Daunesse 06904 Sophia Antipolis Cedex, France

Abstract

This chapter describes the key stages in additive manufacturing using fused filament fabrication. It shows that heating and melting are a compromise between heat transfer from the extruder and polymer transport. Pressure drop and the force required for extruding the filament are reported. The morphology of extruded threads depends on extrusion and printing velocities, the distance between the nozzle and the deposit, and the nozzle diameter. Post-deposition cooling and the crystallization of semi-crystalline polymers are studied. Thread-to-thread interactions are presented, focusing on cooling and welding.

Keywords: Polymer, 3D printing, Fused Filament Fabrication, heat transfer, fluid mechanics, finite element method.

Contents

*Corresponding author: Tel. +33 (4) 93 95 74 34

Email address: franck.pigeonneau@minesparis.psl.eu (F. Pigeonneau)

Preprint submitted to 10.1016/b978-0-323-95486-0.00125-3 *January 8, 2025*

1. Introduction

According to the ISO/ASTM 52900 standard (ISO/ASTM, 2021) additive manufacturing (AM) encompasses technologies enabling parts to be manufactured using the deposition of successive material layers defined by a digital model. First achievements were made in the late of 1980s to produce prototypes and trinkets. AM is now used for many parts in common use or in high-tech applications. It can be applied to various materials as metals, ceramics, polymers, concrete and, more recently, glass (Datsiou et al.,

2019). Its field of application is growing up all the time, enabling us to produce parts for cutting-edge sectors such as aeronautics, automotive industry, and healthcare.

Of all AM techniques, 3D printing using plastic extrusion accounts for a large share of the market. Known as Fused Deposition Modeling (FDM) or Fused Filament Fabrication (FFF), it is easy to set up and requires moderate energy, low-cost materials (thermoplastic polymer filaments) and low investment costs, as compared to alternative (AM) techniques as Selective Laser Sintering (SLS) for instance. Nevertheless, mechanical properties remain below those of products shaped by conventional polymer processing methods. To improve properties and open up even more applications, FFF printers need to be further developed. Material extrusion process has been already reviewed by Turner et al. (2014) with a focus on mathematical process modeling and by Turner and Gold (2015) with a particular attention on the dimensional accuracy and surface roughness. Das et al. (2020) reviewed the conservative balance equations and the numerical methods. Various aspects such as polymer chain orientation, viscoelastic behavior, and crystallization were presented. The aim of this paper is therefore to detail the key stages of the process, drawing on the first principles of physics and process engineering. It is a complementary review of the previous contributions.

Having outlined the process in section 2, the way in which the polymer melts in the extruder is described in section 3. The shape, dimensions and temperature of the deposited strand are then studied in section 4. Section 5 focuses on the printing of parts with multiple strands and on the welding problems of both amorphous and semi-crystalline polymers. Some perspectives on the FFF process will be proposed in section 6.

2. Description of the material extrusion additive manufacturing process

Since the aim of this chapter is not to provide an exhaustive overview of 3D printer technologies, interested readers are referred to Gibson *et al.*'s book (Gibson et al., 2015) which is an important source of information on all additive manufacturing technologies. To introduce the physical phenomena detailed in the following sections, the operating principles of a FFF 3D printer are outlined in this section.

In its principle, the fused deposition additive manufacturing process has marginally

evolved since Crump's patent (Crump, 1992), which led to the first FDM 3D printers marketed by Stratasys in 1992. Nevertheless, the RepRap project (Jones et al., 2011) achieved a significant work to develop open-source 3D printers. After the expiration of FDM printing process patents in 2009, a new wave of industrial companies appeared with the aim to provide commercial FDM 3D printers accessible to the general public. Figure 1 represents the operating principle of a Cartesian FDM 3D printer, along with its essential components.

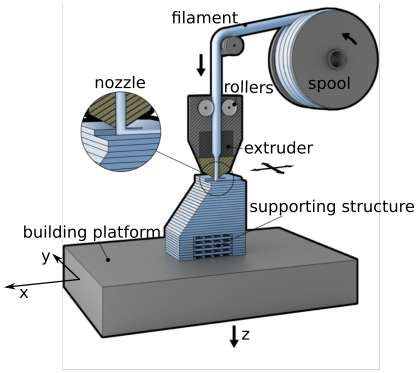

Figure 1: Schematic representation of a Cartesian 3D FDM printer (modified from https://www.manufacturingguide.com/).

The printed part is supported by a platform heated at a controlled temperature, (noted T_{sub} in the remainder of this chapter). As illustrated in Figure 1, to build up the printed object, the platform moves vertically along the z axis. The platform can be also immobile. In this case, the printer head moves, attached to a horizontal carriage. The printer head consists mainly of an extruder, which melts the polymer and extrudes the filament through a nozzle. The feed system consists of a spool delivering a filament at a constant velocity prescribed through rollers. Thanks to a mechanical system, the printer head moves along axes conventionally designated x and y. On printers with vertically fixed platforms, the head moves only along the x axis, while the platform translates along the y axis, simultaneously with its vertical displacement along the z axis when one slice of the part is completed. There is yet another technology, the delta printer, which moves the extruder head along all three axes (Bell, 2015). On the bottom of the part, a support, printed in the same material, can be added, and will be removed for finishing.

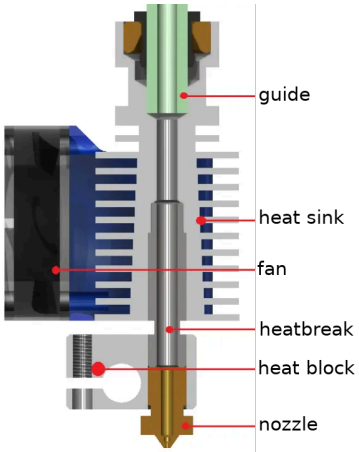

Figure 2: E3D-V6 extruder with main elements: cross-section of the extruder with the main parts [modified from (E3D-online, 2021)].

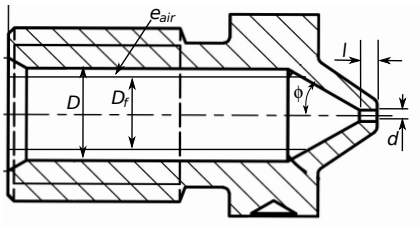

Figure 3: Cross-section of the nozzle with the main dimensions (modified from (E3D-online, 2021)).

The inset on Figure 1 is a zoom on the molten filament deposition after passing through the extrusion nozzle.

As an example, Figure 2 shows the V6 printer head designed by E3D (E3D-online, 2021). The cross-section of the extruder is depicted with the designation of the main parts of the extruder. It is equipped with a nozzle which cross-section is shown on Figure 3.

The nozzle is made up of three parts: upstream a pipe of diameter D, the same size as the heat block in which it is inserted, then a conical part and a small capillary channel whose dimensions (length l and diameter d) vary according to the desired extrudate size. The cone is characterized by the open half angle, ϕ, which is in general equal to $\pi/6$. To more details, dimensions can be found on the Website of E3D (E3D-online, 2021).

The heating element melts the polymer. Energy is provided by means of an electrically

powered cartridge heater. The working temperature T_{ext} is controlled by a thermistor. To heat up the polymer as efficiently as possible, the heat block is generally made of aluminum, a low-cost material with high thermal conductivity. To prevent heat diffusion to the cold section of the extruder and the solid filament upstream, an air exchanger with cooling fins is installed above the heat block. To increase heat exchange, forced convection is ensured by a fan. Finally, a heat breaker is disposed between the heat block and the upper cold section of the printing head.

The main polymers used for this kind of printing are amorphous thermoplastics (such as ABS or PC) or semi-crystalline thermoplastics (such as PLA, PP). These materials have formulations specifically developed for FDM 3D printing. Further information on usable polymers can be found in (Fico et al., 2022). The most common filament diameter D_f is 1.75 mm, but there is also filament diameter of 2.85 mm.

Polymer melting takes place in a channel whose length L is of the order of 17.5 mm. This length corresponds to the upstream channel of the nozzle and the channel of the heat block until the heat break, see Figure 2. For filament diameters of 1.75 mm, the channel has a diameter D equal to 2 mm. An air gap e_{air} of 125 µm is therefore present at the start-up of extrusion between the polymer and the channel.

Based on an STL-type CAD file of the part to be produced, slicing software is used to code the operations to be performed by the printer. The language most used to communicate with the printer is G-code. As the part is made up of slices, the molten extrudate is deposited in planes parallel to the $x-y$ plane. The printing velocity, V, is a variable used to translate the stroke of the extruder head. It is used as a parameter in the slicing software. When a slice has been completely processed, a movement along the z axis is made over a height of the size of the deposited extrudate (referred as thread or strand in the following). The amount of material deposited with each motion is entered as a variable in the G-code file. A mass balance allows to determine the polymer flow velocity at the nozzle outlet, denoted U. Although this data is not required for operation, it is crucial for understanding the thermal limits of the process as it will be presented in 3. Section 4 will show that the U/V ratio is an essential parameter for predicting the size of the deposited strands.

The printed part is thus created by the addition of threads deposited by the extruder

head. To have sufficient mechanical strength of the printed object, the welding between strands is crucial. It is controlled by the cooling undergone by the part during printing and by the pressure exerted by the extruder head during the deposition step. Surrounding air temperature is one of the parameters influencing this cooling process, as well as the amount of heat supplied by the preceding freshly deposited strands below and around the newly deposited one. It is highly dependent on the nozzle diameter: small strands cool down quite quickly and printing parts processed with small diameter nozzles, e.g. 0.15 mm, does not allow correct welding. Shrinkage and crystallization for semicrystalline polymers are other phenomena involved in this consolidation and cooling stage.

This quick overview of how an FDM 3D printer works shows that the polymer goes from solid to liquid in a few seconds, before solidifying again. Non-equilibrium phenomena are therefore at the heart of this process. How does the polymer melt in the extruder head? What is the thermal history of the polymer? How does it vary with extrusion speed at the nozzle outlet? Answers to these questions are essential for the control of the process.

3. Main aspects of the melting and pressure drop in the extruder

3.1. Polymer melting

Filament melting is a key step in the process. The polymer needs to be completely melted at the nozzle outlet. The temperature must be sufficiently high to minimize the pressure drop in the nozzle but not too high to avoid degradation of the polymer. To prevent from filament buckling upstream the heat block and also to have an efficient feeding drive, the polymer has to be in solid state at the inlet of the heat block. For this purpose, a cooled section is introduced in the upstream part of the extruder head.

As it is impossible to see through the heat block, the melting process of the polymer filament remains debated in the literature. Nevertheless, according to Peng et al. (2018), it is conventionally accepted that the polymer enters the heat block in the solid state, its temperature being of the order of that of ambient air, noted hereafter T_0, and that polymer melting takes place in the channel of the heat block (Figure 2) which dimensions, depending on the manufacturer, have been specified in section 2. As the polymer is in motion, heat transfer in the heat block is a combination of thermal conduction and

convection. At the start-up of extrusion, there is an air gap e_{air} between the polymer and the heated duct of the printer.

Pigeonneau et al. (2020) developed a thermo-mechanical model of the filament melting process to reproduce the experimental work of Peng et al. (2018) achieved with a polycarbonate polymer. A numerical simulation of the transport and melting of a polymer is developed by solving the NavierStokes equations coupled to the energy balance. The polymer is seen as a generalized Newtonian fluid with a dynamical viscosity obeying to a Carreau-Yasuda's law (Carreau, 1972; Bird et al., 1987; Agassant et al., 2017):

$$\eta(\dot{\gamma}, T) = \frac{\eta_0 a_T}{\left[1 + (\lambda a_T \dot{\gamma})^a\right]^{(1-n)/a}}, \tag{1}$$

with η_0 is the Newtonian plateau viscosity, n the power-law index, λ a time constant and a a parameter to describe the transition between the Newtonian plateau and the power-law regime. T is the absolute temperature and $\dot{\gamma}$ the generalized shear rate defined by:

$$\dot{\gamma} = \sqrt{2\dot{\boldsymbol{\epsilon}} : \dot{\boldsymbol{\epsilon}}}, \tag{2}$$

with $\dot{\boldsymbol{\epsilon}}$ the rate-of-strain tensor. The time/temperature shift factor a_T obeys to an Arrhenius's law given by:

$$a_T = \exp\left[\frac{E_a}{R}\left(\frac{1}{T} - \frac{1}{T_{\text{ref}}}\right)\right], \tag{3}$$

with E_a the activation energy, R the ideal gas constant and T_{ref} the reference temperature.

For the polycarbonate considered here, the activation energy E_a (see Appendix B) induces a shift factor a_T larger than 10^3 at the glass transition temperature T_g. It increases exponentially at lower temperatures, leading to a very high viscosity and the fluid moves according to a "solid body motion" with a rate-of-strain tensor equal to zero.

At the heat block inlet, the velocity is imposed equal to the filament velocity U_{in} while T is set equal to the temperature T_0. The no-slip boundary condition is imposed at the heating channel wall. As the material of the heating element is a good conductor, it is assumed that the contact temperature inside the channel is equal to T_{ext}, the set temperature of the extruder. To account for the air gap, the thermal boundary condition

follows the Fourier's law (Fourier, 1822) given by:

$$k\frac{\partial T}{\partial n} = \mathfrak{h}_{\text{air}}\left(T_{\text{ext}} - T\right), \tag{4}$$

with k the thermal conductivity of the polymer, $\partial T/\partial n$ the normal derivative of the temperature at the filament surface. Assuming that the thermal resistance in the air gap is a pure conductive transfer through the air gap e_{air}, the heat thermal exchange coefficient h_{ext} between the wall and the polymer can be estimated by:

$$\mathfrak{h}_{\text{ext}} = \frac{k_{\text{air}}}{e_{\text{air}}}, \tag{5}$$

with k_{air} the thermal conductivity of air and e_{air} the air gap. With e_{air} equal to 125 µm, the order of magnitude of this exchange coefficient is $320\,\text{W/K/m}^2$.

Assuming the polymer as incompressible, neglecting the gravity force, and using a usual normalization of balance equations (Bird et al., 1987), the problem is written as follows:

$$\boldsymbol{\nabla}\cdot\boldsymbol{u} = 0, \tag{6}$$

$$\text{Re}\,\frac{D\boldsymbol{u}}{Dt} = -\boldsymbol{\nabla}P + \boldsymbol{\nabla}\cdot\left[2\eta(\dot{\gamma},\theta)\dot{\boldsymbol{\epsilon}}\right], \tag{7}$$

$$\text{Pe}\,\frac{D\theta}{Dt} = \boldsymbol{\nabla}^2\theta + \text{Br}\,\bar{\eta}(\dot{\gamma},\theta)\dot{\gamma}^2. \tag{8}$$

To write these dimensionless equations, the space coordinates are normalized by D, the velocity field by U, the dynamic viscosity by η_0, the pressure P by $\eta_0 U/D$, the shear rate $\dot{\gamma}$ by U/D. Finally, the temperature is writen as follows:

$$\theta = \frac{T - T_0}{T_{\text{ext}} - T_0}. \tag{9}$$

The dimensionless numbers involved in the balance equations are then

$$\text{Re} = \frac{\rho U D}{\eta_0}, \tag{10}$$

$$\text{Pe} = \frac{UD}{\kappa}, \tag{11}$$

$$\text{Br} = \frac{\eta_0 U^2}{k(T_{\text{ext}} - T_0)}. \tag{12}$$

The Reynolds number, Re, is the ratio of inertia to viscous forces, with ρ the density. The Péclet number, Pe with $\kappa = k/(\rho C_p)$, is the ratio of thermal diffusion to advection times and Br, the Brinkman number, is the ratio of viscous dissipation to thermal diffusion energies. For a maximum extrusion velocity U=0.5 m s^{-1}, and the rheology and thermal data of polycarbonate (see Appendix B), the Reynolds number is 2.3×10^{-3}

which means that inertia terms can be neglected in each printing situation. The Péclet number is 7.5×10^3 and the conduction in the flow direction may be neglected in front of the advection. Otherwise, the Brinkman number is of the order of unity and viscous dissipation has to be considered, especially at high extrusion velocity.

The Fourier boundary conditions are then written as follows:

$$\frac{\partial \theta}{\partial n} = \mathrm{Bi}(1 - \theta). \tag{13}$$

Note that the dimensionless temperature of the extruder is equal to 1, eq. (9). The Biot number, Bi, is given by:

$$\mathrm{Bi} = \frac{\mathfrak{h}_{\mathrm{ext}} D}{k}, \tag{14}$$

At low Biot number, the thermal resistance is high, limiting transfer between the heat block and the polymer. In the opposite case, transfer is more efficient. When the Biot number tends towards infinity, the contact between the heat block and the polymer is perfect meaning that the temperature of polymer at the filament surface is equal to T_{ext}. For conventional polymers and printing conditions, the Biot number is of the order of unity if the air gap is present. We shall see later that this air gap, present at the start of printing, disappears in part as the molten polymer rises along the heating chamber.

A continuous Galerkin finite element method is used to solve the Navier-Stokes equations (6-7) in mixed velocity-pressure formulation using a Taylor-Hood element $\mathbb{P}_2 - \mathbb{P}_1$ to satisfy the discrete inf − sup condition (Ern and Guermond, 2021). To ensure the stabilization of the advection term of the energy equation, a discontinuous Galerkin finite element method (Di Pietro and Ern, 2012) has been chosen with a polynomial degree equal to $\mathbb{P}_{2d}$. The time integration is done with a backward differentiation formula at the second-order (Süli and Mayers, 2003, Chap. 12). The numerical solver has been written with the `Rheolef C++` library developed by Saramito (2020).

Temperature fields in °C for three increasing Biot numbers are shown in Figure 4. These results were obtained for a polycarbonate with a glass transition temperature, T_g, of 150 °C at an extrusion velocity equal to $2.25\,\mathrm{m\,min^{-1}}$. To illustrate polymer heating, the isovalue of $T = T_g$ has been plotted in black solid line in Figure 4.

At low Biot number (Bi=1), Figure 4(a), the temperature rise is slow. Much of the polymer remains at a temperature below T_g. The polymer is brought up to the

extruder temperature only at its tip, in the nozzle area, and on a thin surrounding layer. This can lead to flow jamming as the pressure drop becomes too high. On the other hand, reducing the air gap by a factor of ten, i.e. Bi =10, shows that heating is more efficient, Figure 4(b). The isovalue T_g is observed practically at a short distance from the entrance to the heat block. The polymer exits at a temperature close to that imposed by the heating element. If the Biot number is even higher, Figure 4(c), the heating is even better.

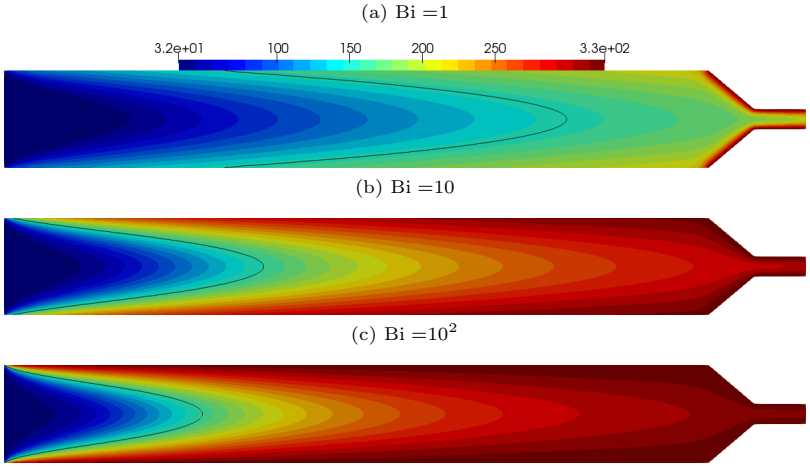

Figure 4: Temperature field (°C) in the heating channel of a 3D printer for three heat transfer coefficients corresponding to Biot numbers (a) Bi =1, (b) Bi =10 and (c) Bi =10^2. The black solid line corresponds to the T_g iso-value.

To record thermal history, Peng et al. (2018) placed a very small thermocouple in a polycarbonate filament prior to extrusion. The crossing of the polymer through the printing head allows to record the thermal history experienced by the polymer. Using the numerical developments summarized above, the temperature rise of the polymer, and especially the temperature obtained at the nozzle exit can be compared to experiments. They carried out their experiments for three extrusion velocities. Figure 5 shows the temperature rise along the channel axis for various values of the Biot number and the extrusion velocities experimented in (Peng et al., 2018).

For all three extrusion velocities, a Biot number of 1 does not reproduce the heating observed experimentally. Consequently, the air gap should be smaller than that given by

the difference between the channel and the filament diameters. It is necessary to have at least a hundred times smaller air gap to have an output temperature close to the experimental data. This means that the air gap disappears along most of the heat block channel as underlined on Figure 6. At the highest extrusion velocity, the temperature obtained numerically remains lower than that observed whatever the Biot number.

The temperature profiles in the capillary at the nozzle exit are plotted as a function of the radial coordinate r for the three extrusion velocities, Figure 5-(d), assuming a perfect contact between the polymer and the heating element, i.e. Bi $= \infty$. At the lowest velocities, the temperature is quite homogeneous in the section of the capillary, whereas an important temperature gradient between the core of the extrudate and the capillary wall is computed at the highest extrusion velocity.

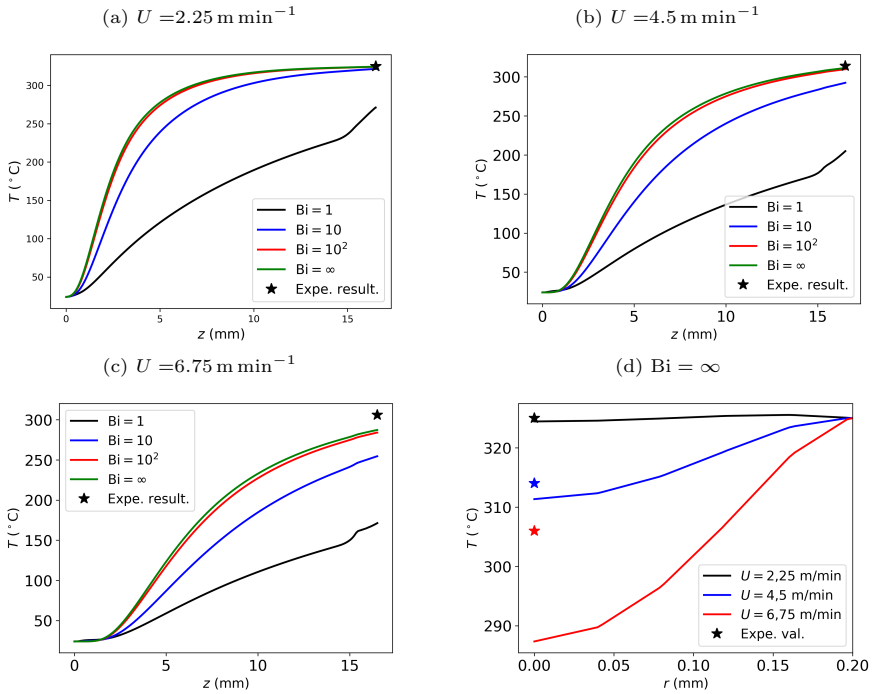

Figure 5: T (°C) as a function of z (mm), on the channel axis for (a) U =2.25, (b) U =4.5 et (c) U =6.75 m min^{-1}. Radial profiles of T are depicted in (d) for Bi $= \infty$ for the three velocities. The symbol $\star$ corresponds to the temperatures recorded by the thermocouple of Peng et al. (2018).

These results underline that a perfect contact between the polymer and the heating element would prevail. Recently, Serdeczny et al. (2020a) have modeled the introduction

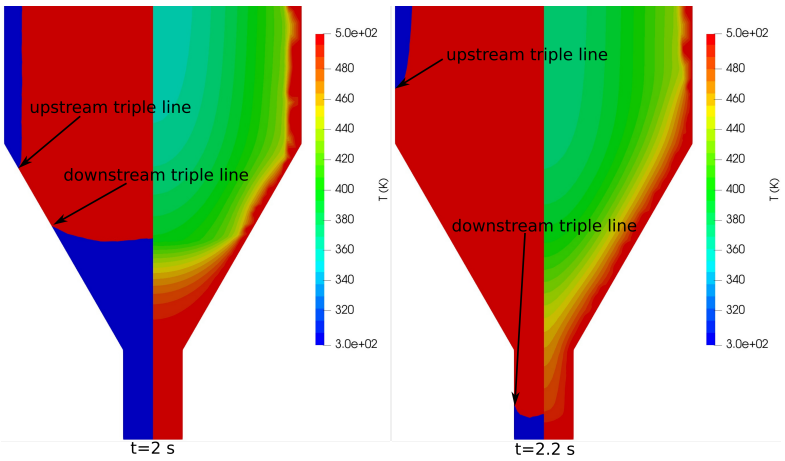

Figure 6: Computational domains filled by air (blue) and polymer (red) on the left-hand side, and temperature given in K on the right-hand side of the symmetry plane at two successive times after extrusion start-up. This example is given for an extrusion velocity $U = 1\,\mathrm{m\,min^{-1}}$.

step of a polymer filament into an E3D-V6 extruder head. The transport of the fluid interface between polymer and air is treated with a Volume-of-Fluid method (Hirt and Nichols, 1981). The dynamics of the entrapped air in the gap between the filament and the heat block can be investigated as well as the polymer spreading on the wall of the heat block. After a transient phase lasting less than a minute, the wall of the heat block is completely wetted by molten polymer and the gap between heat block and filament disappears.

A similar study reported in (Marion et al., 2023) corroborates Serdeczny's previous results (Serdeczny et al., 2020a). A finite element method is used and the fluid interface between the polymer and air is tracked with a level-set method (Sethian, 1999). The governing equations (6)-(8) are completed by a transport equation of the level-set function which will be detailed in subsection 4.2. Figure 6 visualizes the first moments after the start-up of extrusion for $U = 1\,\mathrm{m\,min^{-1}}$ when the polymer filament comes into contact with the extrusion nozzle.

As soon as the polymer, colored in red in Figure 6, is in contact with the nozzle, two triple lines appear, corresponding to the intersection between the polymer, the printing head wall, and the air in blue. The former is localized on downstream of the extruder and disappears quickly after the contact of the polymer with the nozzle. The upstream

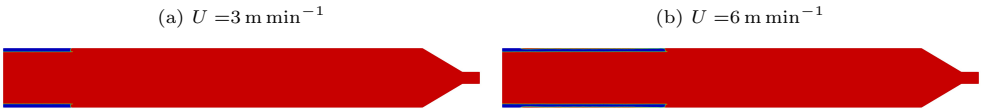

Figure 7: Polymer (in red) inside an extruder obtained by numerical simulation for (a) U=3 m min^{-1} and (b) U=6 m min^{-1}. A layer of air (in blue) persists over a variable length of the extruder in the steady-state regime.

triple line rises as a function of time, due to the reverse flow induced by the pressure build-up in the convergent section of the nozzle and fills progressively the entire gap toward the top of the heat block. The temperature is also plotted on the right part of Figure 6. The radial thermal gradient is large. At the contact between the polymer and the wall, temperature reaches the extruder temperature while the core of the polymer is at a much lower temperature. In the area where the air gap is present, i.e. above the upstream triple line, the temperature at the polymer interface is close to T_g meaning that the polymer is far to be melted at the start-up of extrusion.

When the extrusion velocity is larger than 1 m min^{-1}, the air gap persists close to the inlet of the heat block as it is shown in Figure 7. These two results have been obtained at steady-state regime for two extrusion velocities, U=3 m min^{-1} and 6 m min^{-1}. The air gap has an extension along the heating element that increases with extrusion velocity.

Hong et al. (2022) developed a transparent glass heat block to study the persistence of the air gap. The heating is achieved by a hot air chamber. Experiments are carried out with PLA and ABS. As soon as the polymer comes into contact with the extruder, it takes on the extruder temperature and melts, resulting is a thin layer of molten polymer, which is sharply sheared. On the upper part of the transparent heat block, the air layer persists and acts as a thermal insulator. These observations are in qualitative agreement with Marion et al. (2023)'s numerical simulations. Hong et al. (2022) observed the printed ABS strand at a constant printing velocity V and increasing extrusion velocities U. The strand is smooth at low extrusion velocities which means that it was correctly melted at nozzle exit. It becomes progressively rough and even discontinuous at high velocities which is the signature of an incomplete melting.

3.2. Critical extrusion velocity of melting

It is of interest to develop an approximate model of the filament heating in the heat block. It is akin to the Graetz problem extensively studied in the literature of thermal engineers (Shah and London, 1978). When the polymer is introduced into the heat block, there is a balance between two modes of heat transfer. One is related to convective transport along the longitudinal axis of the heat block, the other to radial heat conduction. The energy conservation equation then takes the following form (Bejan, 2013, Chap. 3):

$$\rho C_p u(r) \frac{\partial T}{\partial x} = \frac{k}{r} \frac{\partial}{\partial r} \left(r \frac{\partial T}{\partial r} \right), \tag{15}$$

with ρ the density of the material, C_p its specific heat at constant pressure and k its thermal conductivity. The velocity $u(r)$ is assumed to be independent of the longitudinal axis, x. As the ratio D/L is small compared to unity, the conduction term in the longitudinal direction may be neglected and equation (15) then takes on a parabolic character according to the classification of partial differential equations (Sneddon, 1957).

One of the criteria for assessing the velocity beyond which extrusion will become difficult is to estimate the velocity at which the polymer exits the nozzle with a temperature of the order of T_g for amorphous polymers (or T_f for semi-crystalline polymers). From equation (15), the limiting velocity for the temperature to be of the order of T_g at the nozzle outlet is written in order of magnitude:

$$u \sim \frac{k}{\rho C_p} \frac{L}{D^2} \frac{T_{\text{ext}} - T_0}{T_g - T_0}. \tag{16}$$

The position L_{T_g} of the iso-T_g on the channel axis was determined numerically in (Pigeonneau et al., 2020) by solving the equations of fluid mechanics coupled with heat transfer, see Figure 5. The velocity profile $u(r)$ now evolves along the heating element. Figure 8 represents the ratio of L_{T_g} to the reduced glass transition temperature as a function of the extrusion velocity expressed in reduced form in terms of the Péclet number, eq. (11). The dimensionless temperature θ_g is defined as follows:

$$\theta_g = \frac{T_g - T_0}{T_{\text{ext}} - T_0}. \tag{17}$$

Figure 8 gathers a series of numerical computations in which three extruder temperature values and two polymers were simulated. A curve of L_{T_g}/θ_g as a function of the

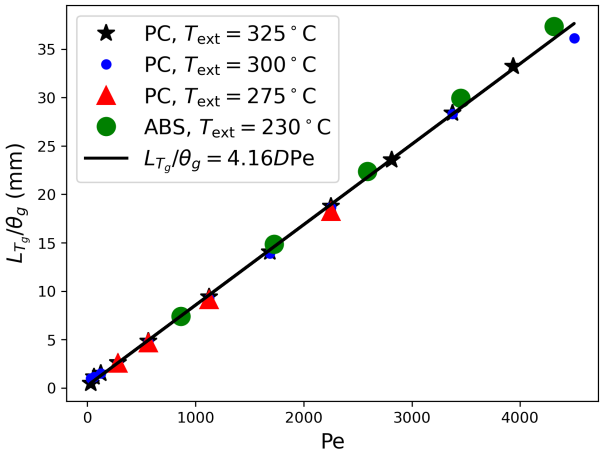

Figure 8: L_{T_g}/θ_g (mm) as a function of Pe for polycarbonate bisphenol-A and ABS.

Péclet number is obtained, enabling us to define the limiting extrusion velocity U_{lim} in $\mathrm{m\,s^{-1}}$ at which the L_{T_g} reaches the end of the heat block as follows:

$$U_{\mathrm{lim}} = 2.41 \cdot 10^2 \frac{T_{\mathrm{ext}} - T_0}{T_g - T_0} \frac{k}{\rho C_p} \frac{L}{D^2}. \tag{18}$$

This shows that the approximate equation (16) is well matched by the equation (18) derived from the numerical model.

Mackay et al. (2017) determined the limit feeding velocity in a LulzBot Taz 4 3D printer for three polymers (ABS, PLA and PLA/PHA). The filament diameter is equal to 2.85 mm, the length of the heating element is equal to 28 mm and its diameter to 3 mm. Figure 9a reproduces Mackay's experimental data. The limit feeding velocity, corresponding to the inlet velocity above which it becomes impossible to extrude a filament, is plotted as a function of the extruder temperature. Increasing the extruder temperature allows to print with larger feeding velocities. PLA and the blend PLA/PHA behave quite similarly, while ABS is shifted toward higher temperatures. This is mainly due to the fact that ABS melts at higher temperature and has twice the thermal capacity of the other two polymers.

To compare with Figure 8, the data of Mackay et al. (2017) (Figure 9a) have been redesigned, using mass conservation and the dimensions of the extruder LulzBot heating element. The ambient temperature has been taken equal to 20 °C. The glass transition

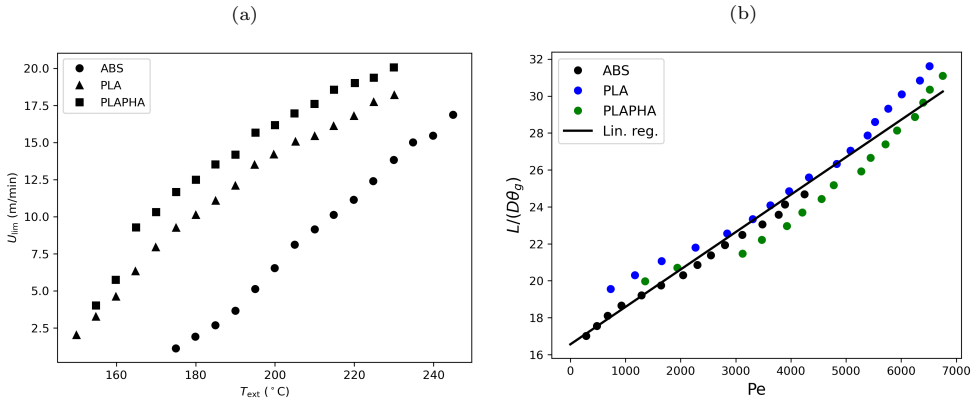

Figure 9: (a) Limit feed velocity as a function of heat block temperature according to Mackay et al. (2017), (b) $L/(D\theta_g)$ as a function of Pe by redesigning data of Mackay et al. (2017).

temperature of ABS has been shifted from 65 °C to 105 °C which is consistent with usual data of literature (Halidi and Abdullah, 2012; Pigeonneau et al., 2020). Figure 9b depicts $L/(D\theta_g)$ as a function of Pe. The general trend is similar to the one obtained Figure 8. The solid black curve in Figure 9b has been obtained by linear regression. It is noteworthy to see that the regression is an affine function (i.e. L is positive for Pe=0) while $L/(D\theta_g)$ deduced from equation (18) and represented in Figure 8 is simply a linear function.

This difference comes from the fact that equation (18) predicts the length where temperature is equal to T_g. This equation accounts well for the effect of the glass transition temperature as well as the effect of the polymer's specific heat. In the experiments of Mackay et al. (2017), the velocity above which it becomes impossible to extrude polymer is determined experimentally. It depends on the temperature at the heating element outlet but also on the pressure which will be needed to extrude the polymer through the conical and capillary sections of the nozzle. This will be addressed in the next section.

3.3. Pressure drop in the printing head

The polymer filament is driven in the printing head by the friction forces exerted by the toothed wheels. The resulting force must overcome the pressure drop in the heating section of the printing head induced by the flow in the nozzle (conical and capillary sections) and in the downstream part of the heat block where the filament is wetted by

molten polymer (see Figure 7). Consequently, there is a maximum pressure drop beyond which the printing process fails. An excessive extrusion pressure may lead, for example, to filament buckling phenomena between the toothed wheels and the printing head inlet.

Bellini et al. (2004) proposed a preliminary description of the pressure drop in the heating section, assuming a constant temperature for the polymer equal to the extrusion temperature. The total pressure drop is the sum of that (I) in the upstream channel of the heating zone, (II) in the convergent section of the nozzle, (III) and in the final capillary section. Assuming a power-law behavior of the dynamic viscosity for the polymer:

$$\eta(\dot{\gamma}, T) = K a_T^n \dot{\gamma}^{n-1}, \tag{19}$$

with $\dot{\gamma}$ already defined in Eq. (2), they obtain analytical relationships for the pressure drop in each flow section as follows

$$\Delta P_I = \frac{4La_T^n K}{D}\left[\frac{2(3n+1)U_{\text{in}}}{nD}\right]^n, \text{ avec } U_{\text{in}} = U\left(\frac{d}{D}\right)^2, \tag{20}$$

$$\Delta P_{II} = \frac{2Ka_T^n}{3n\sin\phi}\left[\frac{3\sin\phi}{4(1-\cos\phi)^2(1+2\cos\phi)}\right]^n\left[\frac{2(3n+1)U}{nd}\right]^n\left[1-\left(\frac{d}{D}\right)^{3n}\right] \tag{21}$$

$$\Delta P_{III} = \frac{4la_T^n K}{d}\left[\frac{2(3n+1)U}{nd}\right]^n, \tag{22}$$

with length L the total extension of the barrel before the cone, D the diameter of the barrel, l the length of the capillary channel of the nozzle with diameter d and ϕ the open half angle of the cone. The different geometry parameters of the heat block are listed on Figure 3.

Figure 10 shows the computed pressure trace along the axis of the heat block for the extrusion of a polycarbonate at three extrusion velocities corresponding to the cases numerically solved in (Pigeonneau et al., 2020). The analytical computations of Bellini et al. (2004) are compared to the numerical thermo-mechanical computations of Pigeonneau et al. (2020) using a Carreau-Yasuda temperature dependent constitutive equation given by equation (1). The rheology and thermal data are listed Appendix B. The two computed pressure values are equivalent in the downstream nozzle region, but the power-law isothermal analytical pressure is significantly higher than the numerical one in the upstream heat block, especially at low extrusion velocity. This is related to the well-known drawback of the power-law constitutive equation which overestimates the

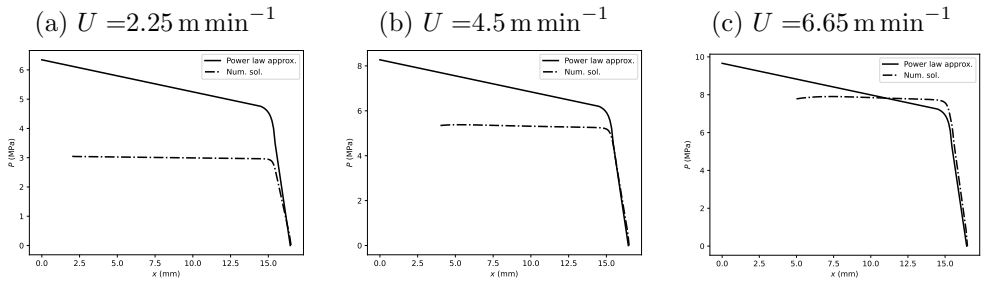

Figure 10: Comparison between analytical pressure trace and numerical one (MPa) for three extrusion velocities. The extruder temperature is set equal to 325 °C.

viscosity at low shear rate whereas the viscosity is constant and equal to the Newtonian plateau value. The difference between both computations decreases at high extrusion velocity because, as it has been shown in subsection 3.1 and in Figure 4, the polymer temperature in the heat block decreases when the extrusion velocity increases, inducing a higher viscosity.

The inlet pressure is of the order of several MPa giving a force of the order of several ten Newtons after integration on the cylindrical section of the printing head. Nienhaus et al. (2019), following Go et al. (2017), measured the feeding force. They used an extruder head, with its cooling system and heat block, mounted on a load cell. A gauge measures the stress generated by the extrusion at a prescribed feeding velocity.

Nienhaus et al. (2019) measured the forces on several printers and for various PLA extrusion velocities. Serdeczny et al. (2020b) did the same kind of measurement for a PLA and a reinforced ABS. Figure 11 reproduced the results of these two contributions. The feeding force is plotted as a function of the feeding velocity, U_{in}, Eq. (20). Both observed a linear increase of the feeding force as a function of the feeding velocity, followed by a sudden increase of the slope at high velocities.

Marion et al. (2023) used the model already presented in subsection 3.1 to compute the extrusion force for ABS printing. The results are in good agreement with the experiments in the low velocity range, but they underestimate the feeding force at the highest velocities which points out the limits of the melting model proposed by Bellini et al. (2004) and numerically implemented by Pigeonneau et al. (2020) and Marion et al. (2023).

Osswald et al. (2018) proposed an alternative model which considers that melting

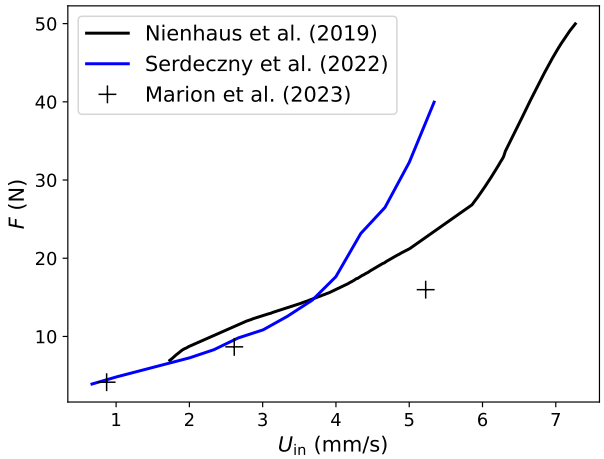

Figure 11: Feeding force required for filament extrusion as a function of filament inlet velocity for an E3D-V6 extruder according to Nienhaus et al. (2019) (PLA), Serdeczny et al. (2020b) (ABS) and Marion et al. (2023) (num. sim. on ABS).

occurs only on a thin layer in the heat block and develops by a sharp squeezing in the convergent section of the nozzle leading to important extrusion forces. This model may be valid at high extrusion velocities and during the start-up period of printing. It could explain the slope increase of the extrusion force at high extrusion velocities observed on Figure 11.

4. Shape of the molten extrudate deposit

The next step of the Fused Filament Fabrication process is the deposition of the extrudate on the building platform and the previously deposited strands. Their width and height will govern the vertical and horizontal displacement of the printing head after completion of the deposition of one layer. The temperature of the fresh deposited strand and the pressure exerted during the deposition step will govern the welding behavior with the surrounding strands and the level of porosity between them. For semi-crystalline polymers, crystallization kinetics within the strands and at the interface between neighbor strands will also govern the final mechanical properties.

4.1. Morphology of the deposited strand

Figure 12 is a view localized close to the tip of the nozzle. The main parameters involved in the deposition of molten extrudates have been indicated. Extrusion and printing velocities, U and V respectively, are the main kinematic parameters. The diameter d of the capillary nozzle and the distance e between the platform (or the previously deposited strands) and the base of the nozzle are expected to be relevant to control the shape and dimensions of deposited strands.

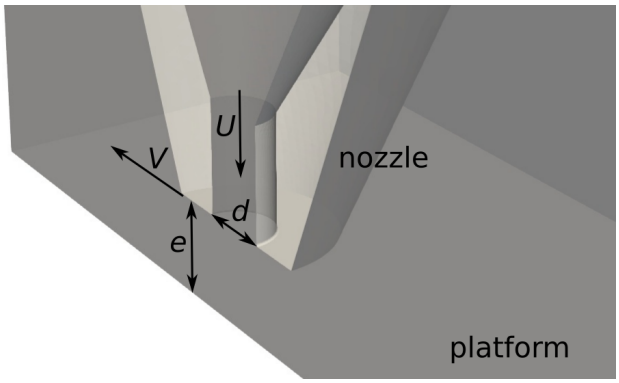

Figure 12: View of the tip of the nozzle close to the building platform with the main parameters involved in the shape of deposited strand.

In the first glance, the area of the cross-section of a deposited strand can be obtained by a mass balance. By neglecting the variation of the specific volume during the strand deposition step, the cross-sectional area $\mathcal{A}$ is given by:

$$\mathcal{A} = \frac{\pi d^2}{4} \frac{U}{V}. \tag{23}$$

Equation (23) has been checked by Hebda et al. (2019) and by Xu (2021). In this last contribution, experiments have been done on a Delta WASP 2040 turbo printer with an ABS polymer. Figure 13 depicts the cross-sectional area A obtained by Xu (2021) as a function of U/V ratio.

The slope of the straight line is directly the cross-sectional area of the filament at the outlet of the nozzle of diameter d=400 µm. As it can be seen in Figure 13, three printing velocities have been used to determine $\mathcal{A}$. These results confirm that the U/V ratio is a natural control parameter of the cross-sectional area. A reduction of the diameter of the

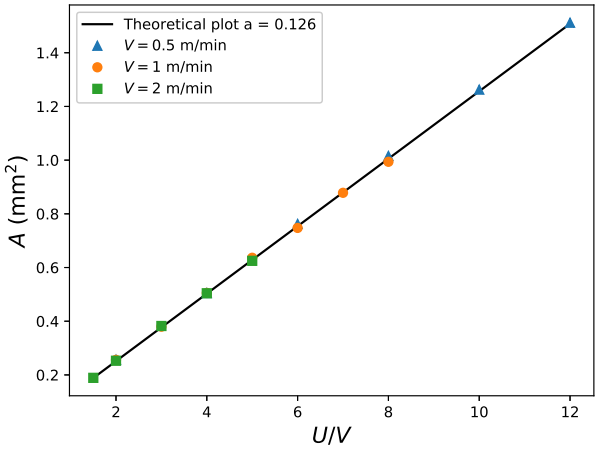

Figure 13: Cross-sectional area $\mathcal{A}$ of the deposited strand as a function of U/V ratio performed with a Delta WASP 2040 turbo printer on ABS polymer. The temperature of the extruder is 230 °C, the temperature of the building platform is 94 °C.

nozzle leads obviously to a decrease of the cross-sectional area which has an influence on the cooling of the deposited strand. The shape of a deposited strand has been studied by Serdeczny et al. (2018), Hebda et al. (2019), and Xu et al. (2021, 2022). Width, height, and shape of a strand cross-section are measured. Models of increasing complexity are then proposed.

4.1.1. Strand width and height of a deposited strand

In Xu et al. (2022), single ABS strands are printed as a function of the U/V ratio for different printing velocities V with a total length of 10 cm. The strand is cut at approximately one half of its length and its shape is observed using an optical microscope. For a given ratio, around ten printed samples are measured. Figure 14a and Figure 14b show the cross-sections of ABS strands obtained for two values of the U/V ratio. They have been printed with a nozzle diameter d equal to 0.4 mm and a gap e equal to 0.6 mm. The shape clearly deviates from a rectangle. The shape of the cross-section is asymmetric: the lower part in contact with the support is flat, while the upper part is more elliptical. The filament width W increases significantly when the extrusion velocity increases. While the gap e is the same between the two experiments shown in Figure 14, the width is two times larger when U/V is equal to 5 than when U/V is equal to 2. Otherwise, the

height H does not change significantly between the two conditions. These cross-section geometries correspond to a case for which e is larger than d.

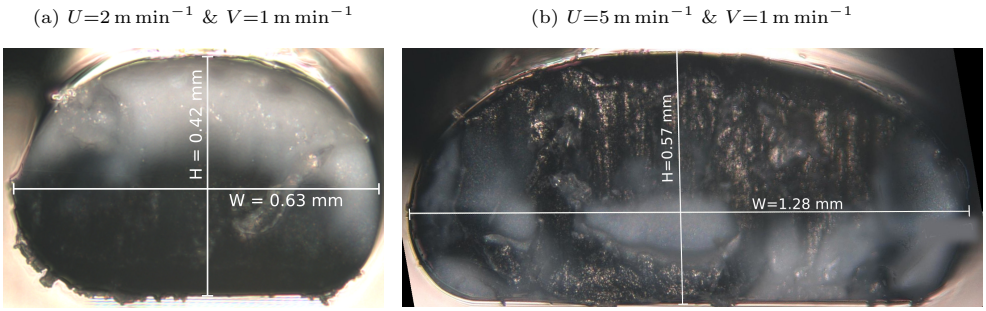

Figure 14: Optical microscopy of ABS strand cross-sections obtained with a nozzle of 0.4 mm and e=0.6 mm for (a) U=2 m min^{-1} & V=1 m min^{-1} and for (b) U=5 m min^{-1} & V=1 m min^{-1} according to Xu et al. (2022).

The determination of the strand shape deposited by the FFF process is a problem of fluid dynamics. A simple dimensional analysis leads to consider the behavior of W/d as a function of e/d, and U/V ratios. Experiments have been done in (Xu et al., 2022) with two nozzles of diameter d equal to 0.4 and 0.3 mm, respectively. The e/d ratio varies in the range of $[0.5; 1.625]$. The velocity ratio U/V is in the range of $[1.5; 5]$. Experiments have been achieved for two values of V. According to Hebda et al. (2019), who performed a similar work, experimental values of W/d behave as a function of $\sqrt{U/V}$. Figure 15 shows that W/d scales linearly as a function of $\sqrt{U/V}$ for each e/d ratio. The decrease of e/d ratio leads to an increase of W/d.

Agassant et al. (2019) developed an analytical model for the strand deposition step of a Newtonian fluid in isothermal conditions. When the gap e is smaller than d, or when the die swell at nozzle exit is important, a squeezing flow between the bottom of the nozzle and the substrate appears. In the (O, x, z) symmetry plane, and in a frame affixed to the moving substrate platform as schematized in Figure 16a, the polymer is sheared between the nozzle and the moving substrate.

At the nozzle outlet, the pressure is P_0 and decreases to atmospheric pressure at the printing head periphery for $x = r_e$. Pressure decreases also to atmospheric pressure in the forward direction at $x = l_f$, which is an unknown of the problem. The superposition of these shear and pressure flows will be responsible for the development of a pressure

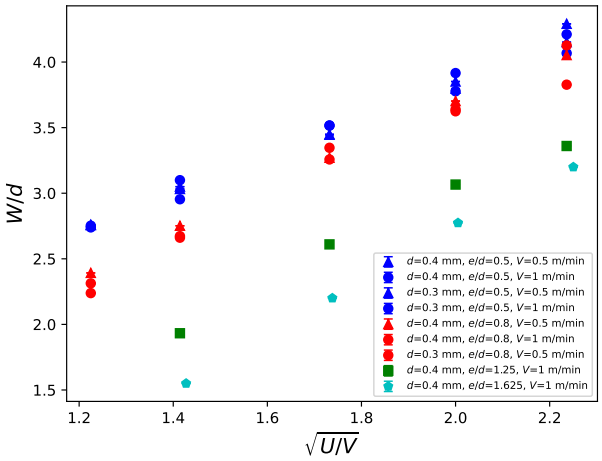

Figure 15: W/d as a function of $\sqrt{U/V}$ obtained experimentally for two printing velocities, two nozzle diameters and four e/d ratios.

field. In the deposit direction, i.e. for $x < 0$ in Figure 16a, the Stokes equations give the deposit rate per unit width q as follows:

$$q = \frac{eV}{2} + \frac{P_0 e^3}{12\eta(r_e - r)}. \tag{24}$$

It is the sum of a simple shear flow induced by the velocity V and a pressure flow induced by P_0 on a distance r_e–r. Equation (24) relies on the fact that the polymer remains in contact with the bottom of the printing head up to $x = -r_e$. In the forward direction, i.e. $x > 0$ in Figure 16a, the flow rate per unit width is nil and is the sum of the same

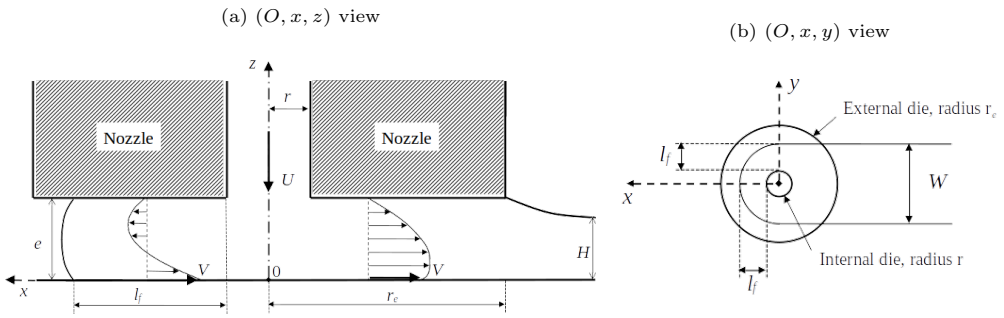

Figure 16: Flow between the bottom of the nozzle and the building platform: (a) (O, x, z) view and (b) (O, x, y) view.

shear flow and of a negative pressure flow induced by P_0 on a length l_f:

$$\frac{eV}{2} - \frac{P_0 e^3}{12\eta l_f} = 0, \tag{25}$$

This leads to the value of l_f:

$$l_f = \frac{P_0 e^2}{6\eta V}. \tag{26}$$

This 2D model in the (O, x, z) symmetry plane is unable to predict the width of the deposited layer. Assuming that the polymer spreading in the direction y perpendicular to the (O, x, z) plane is of the same order of magnitude as the spreading in front of the nozzle, see Figure 16b, leads to an approximate value of the strand width $W = d + 2l_f$. This corresponds to an axisymmetric Stefan flow around the nozzle. Numerical solution of the polymer spreading developed in subsection 4.2 will validate this assumption.

Assuming that the flow rate is uniform through the width, which means that the thickness of the deposited layer is also uniform, leads to:

$$q = \frac{Q}{(d + 2l)} = \frac{eV}{2} + \frac{P_0 e^3}{12\eta\,(r_e - r)}. \tag{27}$$

By substituting in Eq. (27) P_0 by its value derived from Eq. (24) leads to an equation of second order in the variable l_f which has only one positive root:

$$l_f = \frac{-r_e + \sqrt{(r_e - d)^2 + \frac{\pi d^2 U}{eV}\,(r_e - r)}}{2}. \tag{28}$$

It is noticeable that l_f is only dependent on the geometry of the nozzle and on the printing parameters. Therefore, W/d is given by

$$\frac{W}{d} = 1 - \frac{r_e}{d} + \sqrt{\left(\frac{r_e}{d} - 1\right)^2 + \frac{\pi d U}{eV}\left(\frac{r_e}{d} - \frac{1}{2}\right)}. \tag{29}$$

According to the geometry characteristics of the nozzle (E3D-online, 2021), the first term, $(r_e/d - 1)/2$, in the square root is much less than the second term. It can thus be neglected as a first approximation. The strand width is expected to depend predominantly on:

$$\alpha = \frac{U}{V}\frac{d}{e}. \tag{30}$$

Serdeczny et al. (2018) did experiments to measure the width and height of deposited PLA strands on a BQ Hephestos 2 printer. Hebda et al. (2019) did several experiments

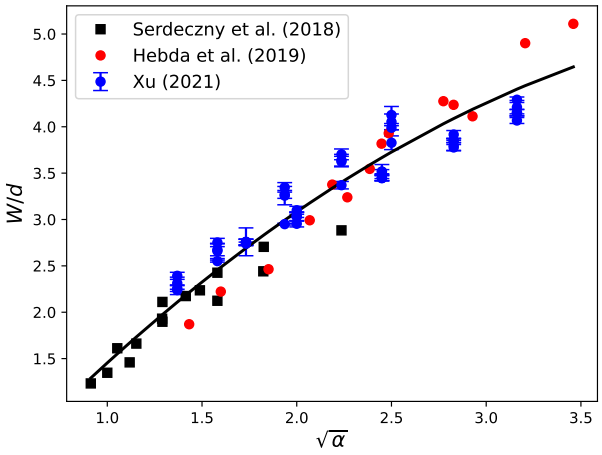

Figure 17: W/d as a function of $\sqrt{\alpha}$ of experimental data from Serdeczny et al. (2018), Hebda et al. (2019) and Xu et al. (2022).

to determine strand morphology on a MakerBot Replicator 2 printer for ABS and PLA. Various e/d ratios were investigated in both contributions. Xu et al. (2022) carried their experiments on a Delta WASP 2040 turbo printer for ABS. The printers used in these three studies have each their own particularities. The BQ Hephestos 2 printer is based on RepRap technology developed by Jones et al. (2011). The MakerBot Replicator 2 printer features a z moving platform, while the WASP 2040 turbo printer operates with a head that moves in all three spatial directions. The W/d ratio is plotted in Figure 17 as a function of α for the three sources of data.

Although these data came from different experiments and were obtained on printers of different technologies, the agreement is satisfactory and shows that $\sqrt{\alpha}$ is indeed the relevant parameter to determine W/d. At low $\sqrt{\alpha}$, W/d varies linearly in $\sqrt{\alpha}$. Its evolution is parabolic at higher $\sqrt{\alpha}$. A fitting solution has been determined from all data, plotted in Figure 17 in solid black line. The fitting law is given by:

$$\frac{W}{d} = -0.63 + 2.31\sqrt{\alpha} - 0.23\alpha. \tag{31}$$

The knowledge of the strand width leads to the determination of its height through the mass balance and assuming an elliptic strand shape (Hebda et al., 2019):

$$\frac{H}{d} = \frac{U}{V}\frac{d}{W}. \tag{32}$$

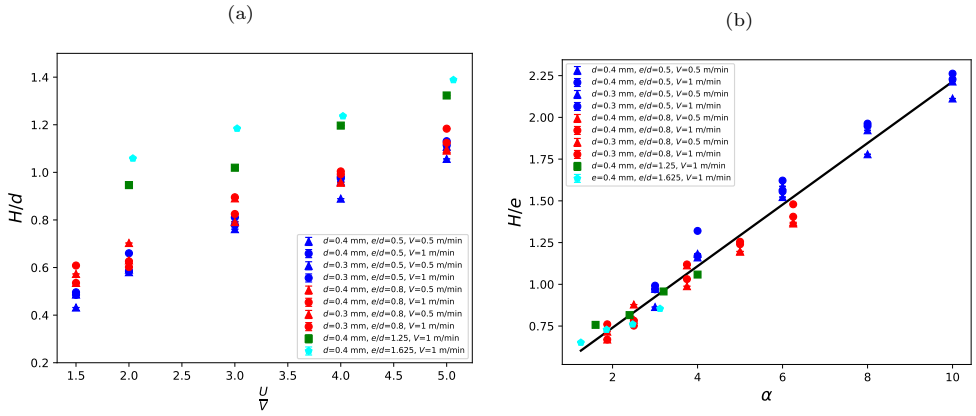

Figure 18: Experimental data given the height of deposited strands in (a) H/d vs. U/V and (b) H/e vs. α.

Figure 18a depicts the H/d ratio as a function of U/V for different e/d ratios obtained experimentally by Xu (2021), see also (Xu et al., 2022). A linear trend of H/d as a function of U/V appears. The height of the strand increases with e/d ratio with the same explanation as for the strand width. When e/d is lower than one, the strand is squished between the substrate and the nozzle. When e/d is larger than one, the strand height is free to develop. The dispersion for the various e/d values is large which limits the possibility to find a general synthesis of these data.

Equation (32) allows to write H/e as follows:

$$\frac{H}{e} = \frac{d}{e}\frac{U}{V}\frac{d}{W} = \alpha\frac{d}{W}. \tag{33}$$

Since W/d is a function of α, it is expected to find a scaling of H/e as a function of the same parameter. Figure 18b provides H/e as a function of α showing a linear behavior. The black solid line represents the solution obtained by a linear regression given by:

$$\frac{H}{e} = 0.5944 + 0.1425\alpha. \tag{34}$$

The knowledge of the strand width and height is of prime importance for the setting of the deposition path to build an object with the desired infill. The empirical model gives a good first approximation of the strand height. The discrepancies between experimental data and equation (34) do not exceed 16 %.

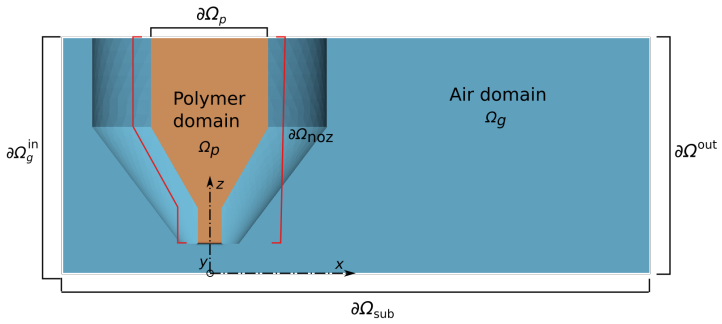

Figure 19: Partial view in the symmetric plane of the domain in the initial state with the two subdomains and the main boundaries.

4.2. Numerical computation of the strand shape

4.2.1. Problem statements and numerical method

The numerical investigations achieved with our own finite element `C++` library (Ville et al., 2011; Silva et al., 2012) focus on the polymer spreading below the printing head. The polymer is considered as a temperature dependent generalized Newtonian fluid. The dynamic viscosity is given by the Carreau-Yasuda's law, eq. (1). Since the process is achieved in an open system, the overall pressure does not significantly change the air density. Moreover, the thermal gradients are not strong enough to consider thermal dilatation of the surrounding air. The reference frame is attached to the nozzle. The motion is considered by sliding the substrate in the opposite direction of the motion of the extruder. Figure 19 shows the cut in the symmetric plane of the computational domain. The geometry of the nozzle is taken from the design of the E3D-V6 nozzle (E3D-online, 2021). Initial positions of the polymer and air domains are depicted as well as their main boundaries.

The interface between the two phases is simply given by $\Gamma(t) = \partial\bar{\Omega}_p(t) \cap \partial\bar{\Omega}_g(t)$ (Groß and Reusken, 2011). To follow the polymer and air phases, respectively and the interface $\Gamma(t)$, the two-phase fluid dynamics is described as a single-fluid representation (Kataoka, 1986). Each phase is flagged by a characteristic function. To determine these functions, the position of the interface between the two phases is used by taking the

level-set function defined as follows (Sethian, 1999):

$$\varphi(\boldsymbol{x},t) = \begin{cases} d_\Gamma(\boldsymbol{x}) & \forall\ \boldsymbol{x} \in \Omega_p(t), \\ 0 & \forall\ \boldsymbol{x} \in \Gamma(t), \\ -d_\Gamma(\boldsymbol{x}) & \forall\ \boldsymbol{x} \in \Omega_g(t), \end{cases} \tag{35}$$

in which $d_\Gamma(\boldsymbol{x})$ is the Euclidean distance from the interface $\Gamma(t)$. The characteristic function for the polymer is $\mathcal{H}(\varphi(\boldsymbol{x},t))$ corresponding to the generalized Heaviside function. The complementary function $1-\mathcal{H}(\varphi(\boldsymbol{x},t))$ corresponds to the characteristic function of the air subdomain.

Since the work is focused on a scale corresponding to the gap between the bottom of the nozzle and the substrate, the spatial dimensions are scaled by e. The characteristic velocity is the printing velocity, V. All physical properties, density, dynamic viscosity, heat capacity, thermal conductivity are normalized by the properties of the polymer given in Appendix B. The characteristic viscosity is taken on the Newtonian plateau. Using the general method presented in (Kataoka, 1986), the governing equations are the following:

$$\boldsymbol{\nabla}\cdot\boldsymbol{u} = 0, \tag{36}$$

$$\mathrm{Re}\,\rho\frac{D\boldsymbol{u}}{Dt} = -\boldsymbol{\nabla}P + \boldsymbol{\nabla}\cdot[2\eta(\theta,\dot\gamma)\dot{\boldsymbol{\varepsilon}}] + \frac{1}{\mathrm{Ca}}\kappa_\Gamma\delta(\varphi)\|\boldsymbol{\nabla}\varphi\|\boldsymbol{n}_\Gamma, \tag{37}$$

$$\rho C_p\frac{D\theta}{Dt} = \frac{1}{\mathrm{Pe}}\boldsymbol{\nabla}\cdot(k\boldsymbol{\nabla}\theta)\,. \tag{38}$$

Equation (36) means that the volume is conserved. Both polymer and air are then assumed incompressible. Moreover, no mass transfer is considered between the two fluids. In the momentum balance equation (37), gravity forces are neglected since the characteristic scales are small. The last source term in the right-hand side of Eq. (37) corresponds to the surface tension force for which $\delta(\varphi)$ is the Dirac function of φ, see Brackbill et al. (1992). The unit normal at the interface $\Gamma(t)$ and the mean curvature are defined by:

$$\boldsymbol{n}_\Gamma = \frac{\boldsymbol{\nabla}\varphi}{\|\boldsymbol{\nabla}\varphi\|}, \tag{39}$$

$$\kappa_\Gamma = -\boldsymbol{\nabla}\cdot\boldsymbol{n}_\Gamma. \tag{40}$$

The reduced temperature in (38) is given by:

$$\theta = \frac{T-T_{\mathrm{air}}}{T_{\mathrm{ext}}-T_{\mathrm{air}}}, \tag{41}$$

with T_{ext} the extruder temperature and T_{air} the temperature of the surrounding air. In (38), the viscous dissipation has been neglected.

The Reynolds number, Re, the capillary number, Ca, and the Péclet number, Pe are defined by

$$\text{Re} = \frac{\rho_p V e}{\eta_0}, \tag{42}$$

$$\text{Ca} = \frac{\eta_0 V}{\gamma}, \tag{43}$$

$$\text{Pe} = \frac{\rho_p C_{p_p} V e}{k}, \tag{44}$$

$$\text{Wi} = \frac{\lambda V}{e}. \tag{45}$$

The Reynolds and the Péclet numbers are different than the Reynolds and Péclet numbers introduced in Section 3 (Eqs. 10 and 11) because of different space and velocity characteristic dimensions. The dynamic viscosity of the molten polymer fitted by Carreau-Yasuda law takes the following dimensionless form:

$$\eta_p(\dot{\gamma}, \theta) = \frac{a_T}{\left[1 + (\text{Wi}\, a_T \dot{\gamma})^a\right]^{(1-n)/a}}. \tag{46}$$

The Weissenberg number Wi is only used to make the parameter λ of eq. (1) dimensionless. In the capillary number Ca, γ is the surface tension between the polymer and the air taken equal to $2.8 \times 10^{-2}\,\text{N}\,\text{m}^{-1}$ (Bellehumeur et al., 2004).

In absence of mass transfer, the interface $\Gamma(t)$ is a material surface moving at the fluid velocity meaning that the transport of the interface is simply given by the equation

$$\frac{\partial \varphi}{\partial t} + \boldsymbol{u} \cdot \boldsymbol{\nabla} \varphi = 0. \tag{47}$$

Nevertheless, as it is well known, the transport of φ using the previous equation leads to the loss of the Eikonal property of φ, i.e. $\|\boldsymbol{\nabla}\varphi\| \neq 1$ (Sethian and Smereka, 2003). A reinitialisation of the level-set function is then needed after the transport step. Sethian and Smereka (2003) reviewed the various techniques used to do the reinitialisation. Here, the method proposed by Ville et al. (2011) has been selected. For more details, reader is refereed to references (Ville et al., 2011; Bonito et al., 2016; Xu et al., 2022).

To solve the system of equations (36-38) and (47), a time-marching method is used. The temporal derivatives are determined with a finite-difference method at the first order. To ensure the stability of the scheme, an implicit Euler scheme is implemented. The spatial discretization is achieved by a finite-element method. The domain is discretized with linear tetrahedron elements. For Navier-Stokes equations, the discrete

inf−sup condition is satisfied by using the element $\mathbb{P}_1-$bubble/$\mathbb{P}_1$ (Ern and Guermond, 2004). The temperature and level-set transport equations are stabilized by a Streamline Upwind/Petrov-Galerkin method (Brooks and Hughes, 1982). The polymer/air interface must be defined with the most accuracy. An anisotropic adaptive meshing is achieved. The sharp gradients are captured using an *a posteriori* error estimation based on the length distribution tensor approach and the associated edge based error estimator [see (Jannoun et al., 2015), for more details]. The mesh adaptation is performed after each time step.

Initially, the polymer domain is immersed in the computation domain by incorporating a mesh fitting with the geometry of the nozzle. A level-set function is then created based on the immersed domain. The temperature is then imposed in the polymer and air domains based on the level-set function. The viscosity of the polymer at rest is then computed using the temperature dependence.

At each time step, the polymer viscosity is computed based on the temperature and rate of strain fields of the previous time step. The generalized Navier-Stokes equations are then solved with the material properties corresponding to their respective domains, based on the level-set function computed at the previous increment using a regularized Heaviside function. The heat transfer equation is then solved. The level-set function is transported based on the computed velocity field. Finally, the mesh adaptation is done. The computation stops when the geometry of the deposited strand is stabilized.

4.2.2. Spreading dynamics for two e/d ratio

The polymer spreading of an ABS is carefully analyzed when e/d is equal to 0.75 and 1.625. Numerical computations are achieved for a nozzle diameter equal to 0.4 mm and a printing velocity V equal to $1\,\mathrm{m\,min^{-1}}$. The substrate, the nozzle and the air temperatures are taken equal to 94, 230 and 40 °C, respectively. The physical properties of ABS are listed in Appendix B.

The Reynolds, capillary, Péclet and Weissenberg numbers are summarized in Table 1 for the set printing conditions and the physical and rheological data of ABS. The dimensionless numbers show that inertia and surface tension have a weak effect.

Figure 20 shows the polymer spreading at three successive time steps with e/d equal to 0.75 and U/V equal to 3. Blue and red colors correspond to the surrounding air

Table 1: Values of dimensionless numbers for the two numerical simulations.

e/d	0.75	1.625
Re	2.77×10^{-6}	3.60×10^{-6}
Ca	1748.5	1748.5
Pe	84.17	109.42
Wi	1.78	0.82

and the polymer phases, respectively. The first column of Figure 20 represents the view in the symmetry plane, (O, x, z) while the second column is the view in the (O, y, z) plane perpendicular to the symmetry plane. The well captured interface results from the refined mesh adaptation around the interface performed at each time step. The numerical computation thus allows to study the behavior of the interface with high accuracy.

The first time-step corresponds to the contact of the polymer with the substrate. The extrudate exhibits a quasi-axisymmetric shape. A slight die swell is observed even if the viscoelastic behavior is not accounted for. This corresponds to the die swell of a purely viscous fluid without gravity and inertia effects (Gavis and Modan, 1967). For t=1.863 $\times 10^{-2}$ s, the polymer is drawn by the substrate. Due to a large value of U/V, a slight spreading of the polymer is observed upstream to the deposition (Figure 20 left). The polymer spreads transversely (Figure 20 right). When t=5.643 $\times 10^{-2}$ s, the polymer is in contact with the nozzle and the substrate. At the same time, the polymer spreading upstream is stabilized. The squeezing of the polymer is important for this set of working conditions. However, the polymer spreading upstream does not flow beyond the edge of the printing head. In that case, it could disrupt the displacement of the printer head.

For this first set of working conditions, Figure 21 shows the shape of the strand in the three planes (O, x, y), (O, x, z) and (O, y, z) in the steady-state regime. It is established when the shape of the strand does not change with time. It is reached for t equal to 0.388 s corresponding to a deposition length of around 6.5 mm. The polymer remains in contact with the base of the printing head. It spreads radially from the extruder axis over a radius equal approximately to 0.5 mm, in agreement with the approach developed in (Agassant et al., 2019). The analytical solution of the length l_f given in Equation (28) is equal to 0.37 mm while the numerical computation gives a value of 0.39 mm, i.e.

(a) t=5.13 $\times$ 10^{-3} s

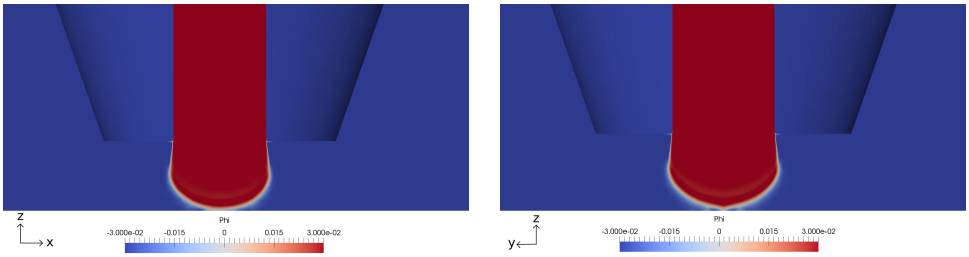

(b) t=1.863 $\times$ 10^{-2} s

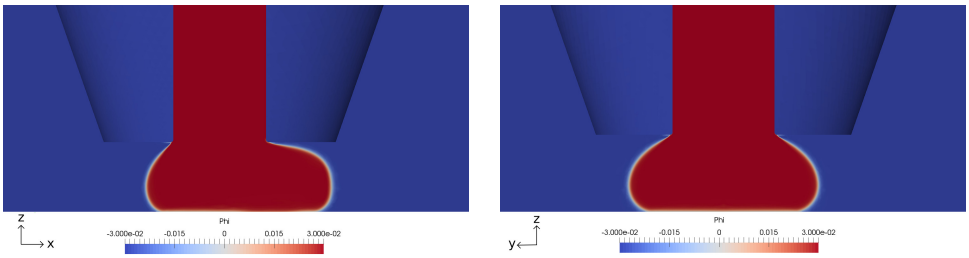

(c) t=5.643 $\times$ 10^{-2} s

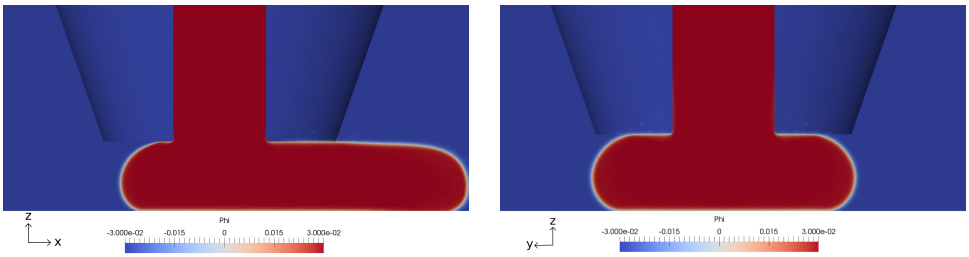

Figure 20: Snapshots of the polymer spreading at the exit of the nozzle at the first steps of the deposition for e/d=3/4 and U/V=3. The first column corresponds to the view in the symmetric plane and the second column, to the view in the transversal (O, y, z) plane.

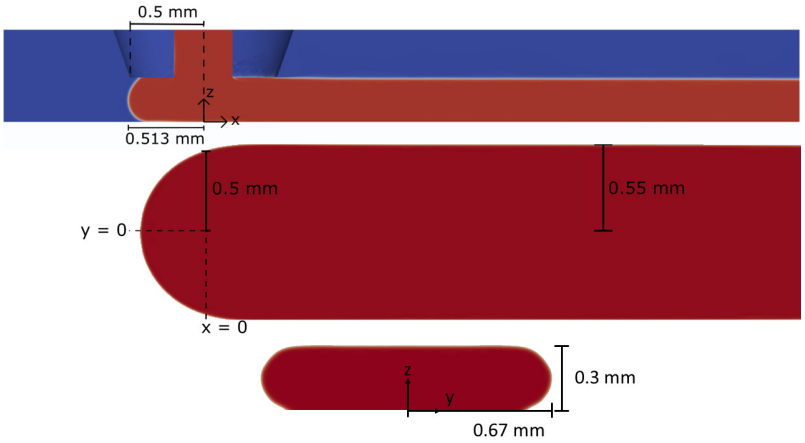

Figure 21: Geometry of the polymer strand for e/d=0.75, U/V=3 for d=0.4 mm and V=1 m min^{-1} in the steady-state regime.

a deviation of 6 % for e/d=0.75. Far from the extruder, the strand spreads wider than the exterior size of the tip of the nozzle. The shape of the strand is very similar to an oblong shape with a height approximately equal to the gap e.

The successive deposition steps when e/d=1.625 are shown in Figure 22. At t=4.036$\times$ 10^{-2} s, Figure 22(b) shows that the polymer is already drawn by the substrate. The contact area is very limited in the (O, y, z) plane as it is clearly seen in the (O, x, z) symmetry plane. For t=8.716 $\times$ 10^{-2} s, the contact area in the (O, y, z) plane remains moderate. When e/d is larger than one, the polymer is not confined between the substrate and the nozzle. The polymer does not touch the base of the nozzle.

Figure 23 depicts the steady-state regime of the strand reached after 0.647 s. This corresponds to a deposition length of 1 cm. The transverse spreading is weak because the extruded polymer is not restrained by the nozzle anymore. The same trend is observable upstream, at the front of the nozzle. In the steady-state regime, the strand shape is close to a half disk around the nozzle and then reaches a uniform shape downstream.

In the $(0, x, y)$ plane, the dimension of the half disk shaped deposit in front of the printing head decreases when e/d increases. Otherwise, in each printing situation, a stabilized deposit shape is achieved within few millimeters, but the transition to the steady-state dimensions occurs on a longer distance when the e/d ratio increases.

The gap distance has an impact on the dimensions and geometry of the deposited

(a) t=1.696 $\times$ 10^{-2} s

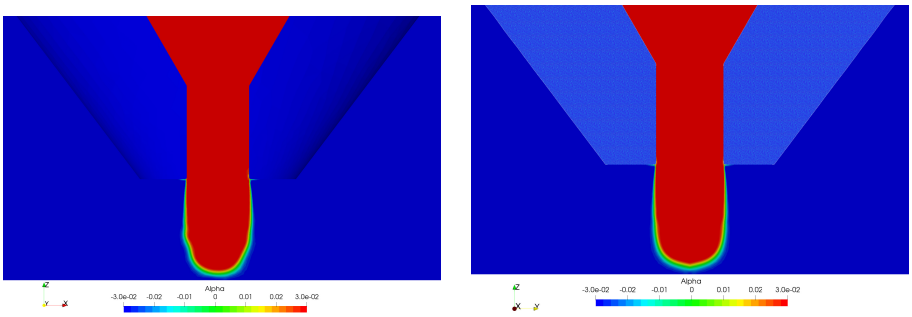

(b) t=4.036 $\times$ 10^{-2} s

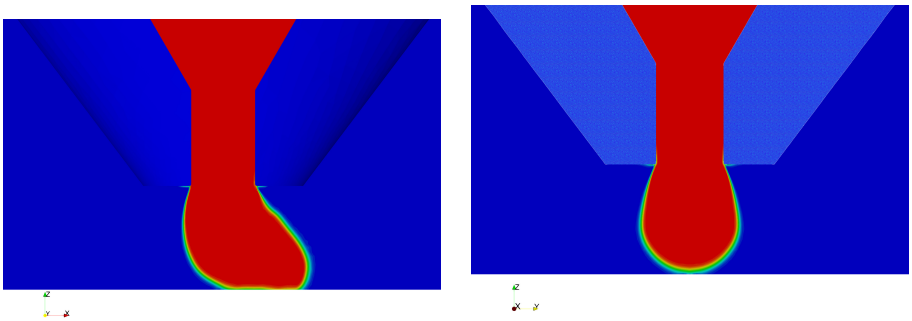

(c) t=8.716 $\times$ 10^{-2} s

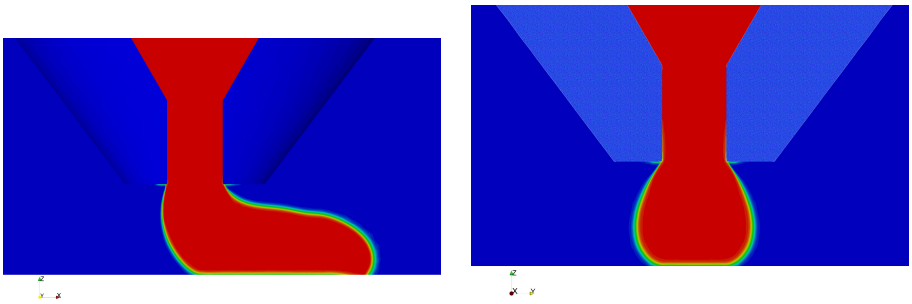

Figure 22: Snapshots of the polymer spreading at the exit of the nozzle at the first steps of the deposition for e/d=1.625 and U/V=3. The first column corresponds to the view in the (O, x, z) plane and the second one in the (O, y, z) plane.

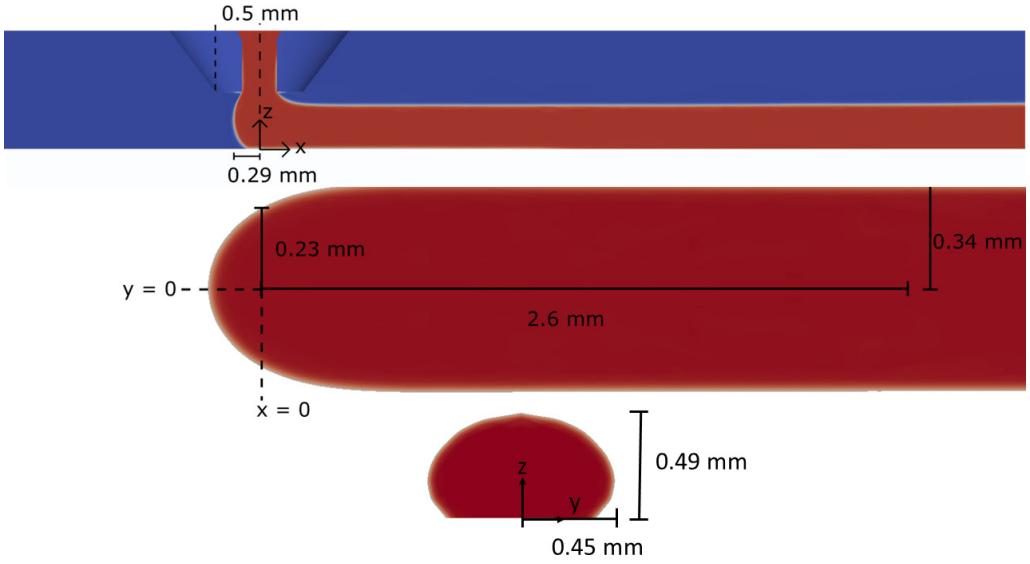

Figure 23: Geometry of the polymer strand for e/d=1.625, U/V=3 for a nozzle diameter equal to 0.4 mm and V=1 m min^{-1}.

strand. For a given printing ratio U/V, the shape is more oblong when the gap is smaller than the nozzle diameter as the polymer is in contact with the nozzle bottom wall. The resulting strand shape has a more planar upper surface. When the gap is more important than the nozzle diameter, the shape is more ellipsoidal.

As seen in Figure 21, for e/d equal to 0.75, the strand maximum height is very close to the gap, i.e. 0.3 mm, and the width is 1.33 mm. On the other hand, for e/d larger than one, the gap does not impact so much the strand shape. In Figure 23, H is equal to 0.49 mm and W=0.9 mm.

4.2.3. Comparison between numerical and experimental predictions of strand dimensions

The computed width W and height H are compared to experimental measurements. The printing velocity V is equal to 1 m min^{-1}. The nozzle diameter is equal to 0.4 mm. The substrate, the nozzle and the air temperatures are set to 94, 230 and 40 °C, respectively.

In Figure 24, the strand shape obtained numerically is compared with the experimental one printed at U/V equal to 2 and e/d equal to 1.625. The cross section of the

(a) Experiment

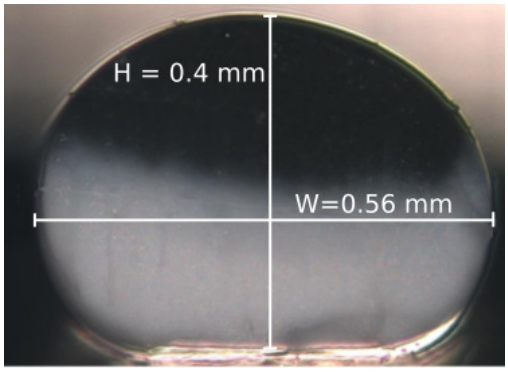

(b) Num. simul.

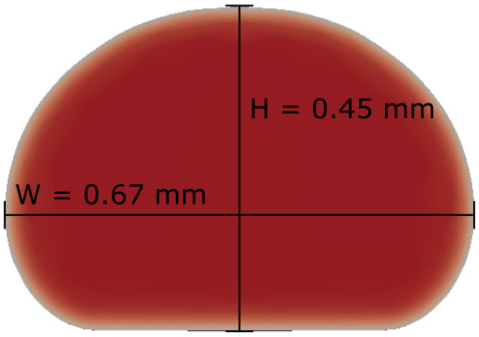

Figure 24: Experimental (a) and numerical (b) cross sections obtained for U/V equal to 2 and e/d equal to 1.625.

(a) Experiment

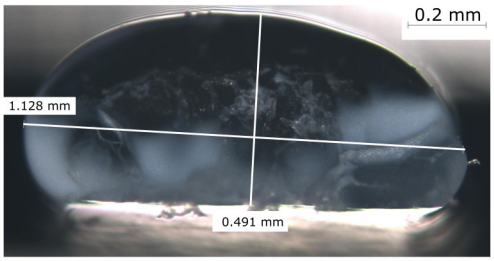

(b) Num. simul.

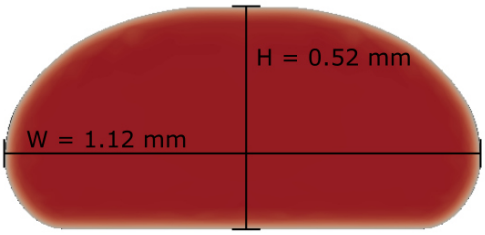

Figure 25: Experimental (a) and numerical (b) cross sections obtained for U/V equal to 4 and e/d equal to 1.625.

deposited strand presents an asymmetric cross section. While the bottom part in contact with the substrate is very similar to an oblong shape, the upper part is more similar to an elliptic shape. This asymmetry is numerically very well captured. The numerical result overestimates both the width and the height of the strand cross section because it does not account for the variation of the density between extrusion (230 °C) and ambient temperature.

An equivalent comparison is done in Figure 25 for U/V equal to 4 and the same e/d ratio. The strand is wider and higher than for U/V equal to 2. The asymmetric cross section and the dimensions of the strand are very well reproduced numerically.

Figure 26a depicts W/d as a function of $\sqrt{\alpha}$ with α defined by equation (30). Both

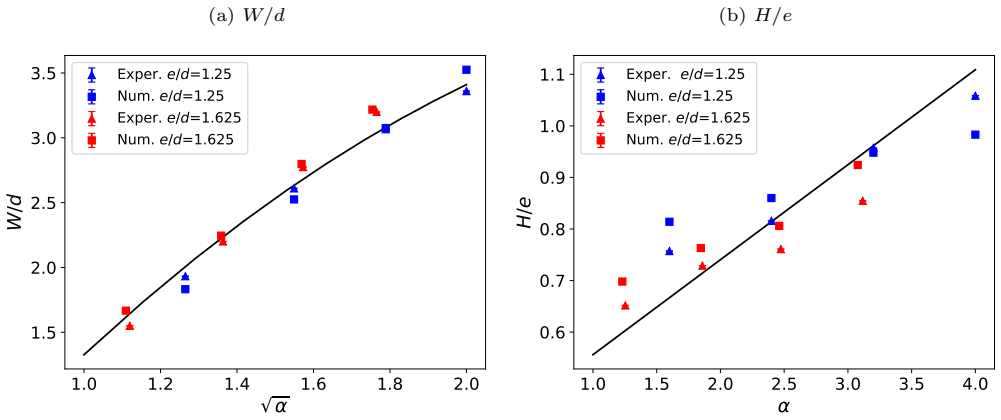

Figure 26: (a) W/d vs. $\sqrt{\alpha}$ and (b) H/e vs. α obtained numerically and experimentally for e/d equal to 1.25 and 1.625.

experimental measurements and numerical computations have been collected for e/d equal to 1.25 and 1.625 in blue and red colors, respectively. The average deviation between the simulated strand width and the experimental measurements is around 5 %. The black solid line corresponds to the approximate solution given by equation (31).

Figure 26b depicts H/e as a function of α for the same series of data. The deviation ranges from 1 to 8 % with an average deviation of 5.9 %. The black solid line is the fitted function given by equation (34). It is less relevant than the width prediction.

4.3. Pressure field

The numerical model gives access to the pressure P exerted on the substrate during the deposition step. The pressure field is depicted in the (O, x, y) substrate plane in Figure 27 for both gaps. When the ratio e/d is equal to 0.75, the pressure field is radially distributed around the axis of the extruder. This means that the flow due to the extrusion is not far from a Stefan-like flow as proposed in Figure 16. When the ratio is lower than one, the extrudate is squeezed between the bottom of the printing head and the substrate. This creates a pressure as high as 0.65 MPa at the nozzle outlet. For e/d equal to 1.625, the pressure at nozzle outlet is 8.8 times smaller than in the preceding case and the pressure field is strongly different. It is to notice that, when printing viscoelastic polymers, an important die swell will be observed at nozzle exit and the squeezing effect will be observed even for e/d ratios higher than one.

(a) e/d=0.75

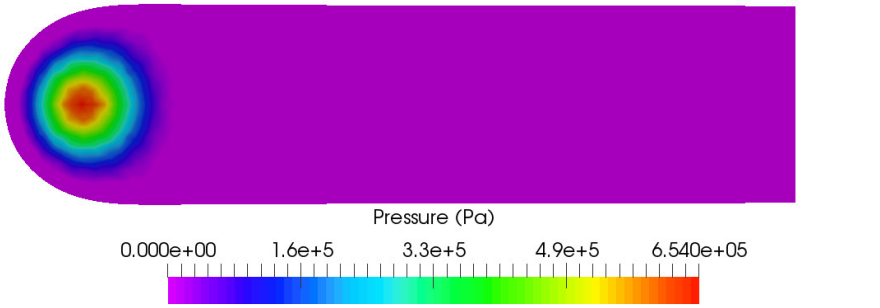

(b) e/d=1.625

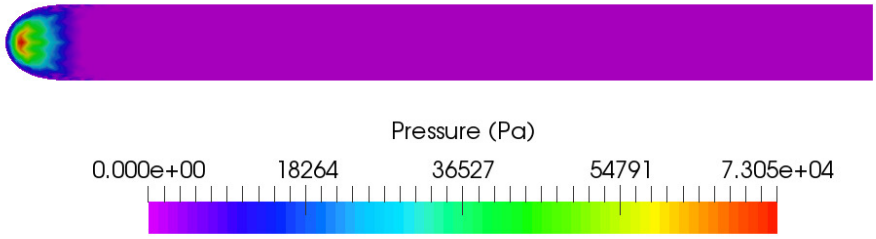

Figure 27: Pressure field in the (O, x, y) plane for (a) e/d=0.75 and (b) e/d=1.625.

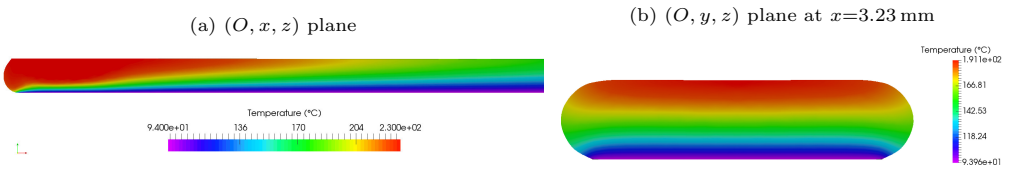

Figure 28: Temperature field for e/d=0.75 (a) in the symmetric plane (O, x, z) over a distance of 7 and (b) in a cross section at x=3.23 mm from the exit of the nozzle.

When e/d=0.75 the pressure will favor welding (Yang and Pitchumani, 2002) and decrease porosity. When e/d=1.625, the contact of the nozzle with the polymer is strongly reduced in the detriment of welding and porosity removal.

4.4. Cooling of deposited strand

Heat transfer during the strand deposition depends on the cooling with the surrounding air and the contact with the substrate. In the single strand printing situation considered here, the interface temperature between the metallic substrate and the deposited strand will be near the temperature of the substrate due to the large effusivity of the metallic substrate. In the case of the deposition of successive stands, which will be addressed in section 5, the interface temperature will be the arithmetic average between the temperature of the previously and the newly deposited strands. In Figure 28, the computed temperature field is shown in the symmetry plane $(0, x, z)$ over a distance of 7 mm for e/d equal to 0.75 and in the cross section localized at x=3.23 mm from the nozzle exit. While the temperature is supposed uniform at the nozzle outlet and near the extrusion temperature T_{ext}, the contact with the substrate leads to a significant cooling. As a result, the strand undergoes an asymmetrical cooling from the bottom to the top. This kind of cooling has been already observed by Ravoori et al. (2019) with an infrared camera. In (Ravoori et al., 2019), the cooling is larger than in our case, but the velocity ratio U/V is not specified. The temperature field in the strand cross section decreases progressively in the x direction resulting from the balance between the advection and the thermal conduction through the strand.

Figure 29 provides the temperature field in the symmetry plane (O, x, z) over a distance of 7 mm and in a cross-section localized at x=3.23 mm for e/d equal to 1.625. The temperature decrease is less pronounced when the gap increases.

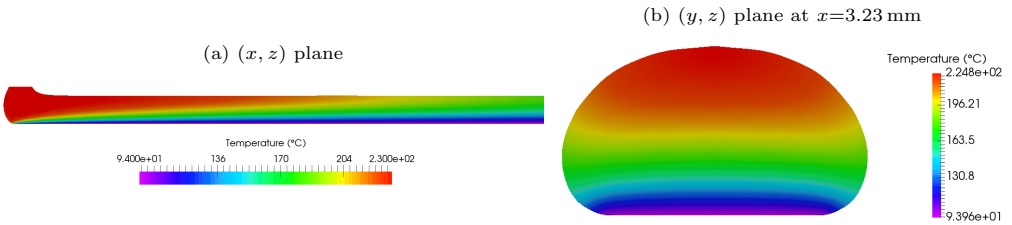

Figure 29: Temperature field for e/d equal to 1.625 (a) in the symmetric plane (O, x, z) over a distance of 7 mm and (b) in a cross section at x=3.23 mm from the exit of the nozzle.

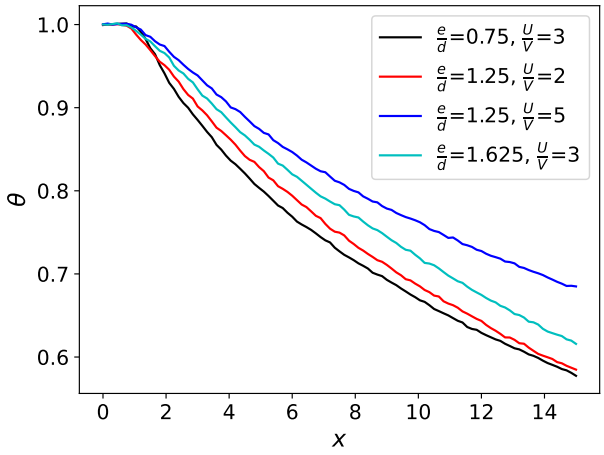

Figure 30: θ taken in the middle of the strand as a function of x.

Numerical computations have been done for other working conditions by changing the gap and the velocity ratio. Figure 30 presents the dimensionless temperature θ for these different printing conditions taken in the middle of the strand as a function of x. After a short area localized under the nozzle where θ is quasi equal to one, cooling is observed along the longitudinal axis, but no clear trend raises as a function of the working conditions of the printer.

The cooling of the strand has been analyzed by Bellehumeur et al. (2004) accounting for the heat transfer between the polymer and the surrounding air and the substrate. It depends on the perimeter $\mathcal{P}$ and the area $\mathcal{A}$ of the cross section. Here the original model of Bellehumeur et al. (2004) is improved by considering the thermal transfer between the polymer and the surrounding air and the polymer and the substrate separately. Using a

1-D description of the deposited strand, the average temperature over a cross section, $\bar{\theta}$, obeys to a simple ordinary differential equation, written under dimensionless form with the characteristic scales introduced in the numerical section:

$$\frac{d^2\bar{\theta}}{dx^2} - \mathrm{Pe}\,\frac{d\bar{\theta}}{dx} - \frac{\mathcal{P}}{A}\left[\chi_{\mathrm{air}}\,\mathrm{Bi}_{\mathrm{air}} + (1-\chi_{\mathrm{air}})\,\mathrm{Bi}_{\mathrm{sub}}\right]\bar{\theta} = -\frac{\mathcal{P}}{A}(1-\chi_{\mathrm{air}})\,\mathrm{Bi}_{\mathrm{sub}}\,\theta_{\mathrm{sub}}, \tag{48}$$

with Pe the Péclet number defined by

$$\mathrm{Pe} = \frac{Ve}{\kappa}, \tag{49}$$

χ_{air} the ratio of the perimeter in contact only with surrounding air to the total perimeter and θ_{sub} is the reduced temperature of the substrate. The two dimensionless numbers, $\mathrm{Bi}_{\mathrm{air}}$, and $\mathrm{Bi}_{\mathrm{sub}}$ are the Biot numbers defined by

$$\mathrm{Bi}_{\mathrm{air}} = \frac{\mathfrak{h}_{\mathrm{air}} e}{k_p}, \tag{50}$$

$$\mathrm{Bi}_{\mathrm{sub}} = \frac{\mathfrak{h}_{\mathrm{sub}} e}{k_p}, \tag{51}$$

with $\mathfrak{h}_{\mathrm{air}}$ air/polymer and $\mathfrak{h}_{\mathrm{sub}}$ polymer/substrate heat transfer coefficients, respectively. Equation (48) is written under dimensionless form with the characteristic scales introduced in the numerical section.

The integration of (48) gives the following solution:

$$\bar{\theta} = \left[1 - \frac{(1-\chi_{\mathrm{air}})\,\mathrm{Bi}_{\mathrm{sub}}\,\theta_{\mathrm{sub}}}{\chi_{\mathrm{air}}\,\mathrm{Bi}_{\mathrm{air}} + (1-\chi_{\mathrm{air}})\,\mathrm{Bi}_{\mathrm{sub}}}\right] e^{-\beta x} + \frac{(1-\chi_{\mathrm{air}})\,\mathrm{Bi}_{\mathrm{sub}}\,\theta_{\mathrm{sub}}}{\chi_{\mathrm{air}}\,\mathrm{Bi}_{\mathrm{air}} + (1-\chi_{\mathrm{air}})\,\mathrm{Bi}_{\mathrm{sub}}}, \tag{52}$$

for $x > 0$ and β given by

$$\beta = \frac{\mathrm{Pe}}{2}\left(\sqrt{1 + \frac{4\mathcal{P}}{A\,\mathrm{Pe}^2}\left[\chi_{\mathrm{air}}\,\mathrm{Bi}_{\mathrm{air}} + (1-\chi_{\mathrm{air}})\,\mathrm{Bi}_{\mathrm{sub}}\right]} - 1\right). \tag{53}$$

Equation (52) suggests that the temperature should be scaled as a function of βx. Figure 31 represents the behavior of the temperature as a function of βx leading to a general curve.

The various values of β have been determined using the data of Pe, $\mathcal{P}$, $\mathcal{A}$, deduced from the numerical results of Figure 30. To obtain this master curve, χ_{air} air is deduced from the computed cross section of the stand, see Figure 28 for example, and then fitted to an oblong shape. The Biot numbers $\mathrm{Bi}_{\mathrm{air}}$ and $\mathrm{Bi}_{\mathrm{sub}}$ have been estimated:

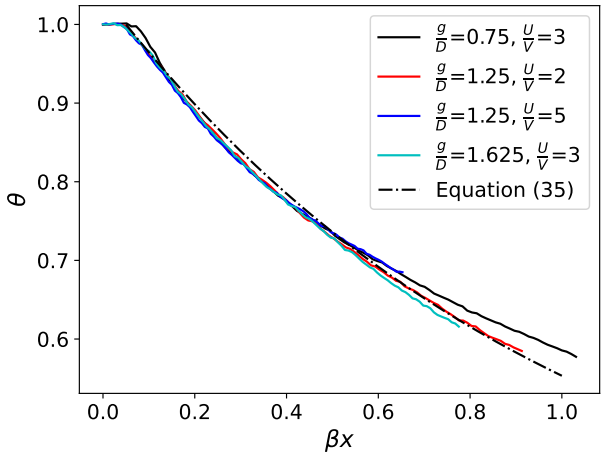

Figure 31: Temperature behavior in the middle of the strand as a function of βx.

According to Agassant et al. (2017, p. 239), the heat transfer due to natural convection for an horizontal cylinder is around $16\,\mathrm{Wm^{-2}K^{-1}}$. The contribution due to thermal radiation is around $13\,\mathrm{Wm^{-2}K^{-1}}$ (Agassant et al., 2017, p. 246). Therefore, the heat transfer coefficient $\mathfrak{h}_{\mathrm{air}}$ between the surrounding air and the polymer strand is set equal to $30\,\mathrm{Wm^{-2}K^{-1}}$ as already used by Thomas and Rodríguez (2000) and by Bellehumeur et al. (2004). The heat transfer coefficient between the polymer and the substrate $\mathfrak{h}_{\mathrm{sub}}$ has been set to $2 \times 10^3\,\mathrm{Wm^{-2}K^{-1}}$.

This simple model pinpoints that the perimeter and the area of the cross section are the relevant parameters to describe the thermal cooling of the deposited strand. With the approximate relations determining the width (Eq. 31) and height (Eq. 34) of a strand, it is possible to study the thermal cooling as developed for instance by Costa et al. (2017).

5. Interaction between deposited strands and solidification of a printed obtect

Up to now, our attention has been focused on the deposition of a single strand. The whole printed object requires the addition of several strands, and it is needed to weld them together to have a cohesive structure. The dimensions of the successive deposited strands are supposed to be identical to the ones analyzed in section 4. However, the temperature field is quite different as the actual deposited strand is in contact with several previously

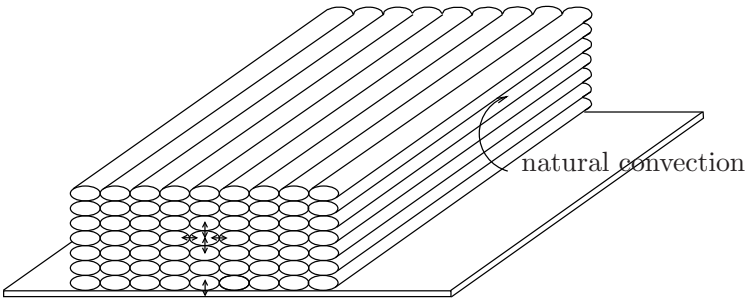

Figure 32: Sketch of the deposition of various layers creating of a printed object. The double arrows mean the thermal transfer by conduction while the circular arrows represent the heat transfer by convection with the surounding air.

deposited ones, which temperature may be quite different than analyzed in subsection 4.4. Once the strand has been deposited, it exchanges heat with the rest of the part being printed and the surrounding air. Unlike processes where heat is supplied by an external heating system, the thermal power in the FDM process comes from each deposited strand (Ravoori et al., 2019). It is given by:

$$\dot{Q} = \rho \frac{\pi d^2}{4} U C_p (T_{\text{ext}} - T_{\text{air}}). \tag{54}$$

When cooling is completed, the final temperature is equal to the ambient temperature T_{air}. The thermal power (Eq. 54) depends on the volume flow rate and therefore on the nozzle diameter d (squared) and the extrusion velocity U and the set temperature T_{ext} of the heat block.

Cooling must be controlled to allow strand-to-strand adhesion. The thermal heat exchange occurs between strands and between strands and surrounding air as illustrated by Figure 32. To simplify, we have represented various strands deposited in the same direction on the building platform. Exchanges by conduction are symbolized by the double arrows and occur between strands and between them and the deposition plane. Exchanges with ambient air are governed by natural convection. All these exchanges determine the overall cooling of the part being printed.

Below, the cooling of a simple wall is studied experimentally and numerically before investigating the welding of amorphous and semi-crystalline polymers.

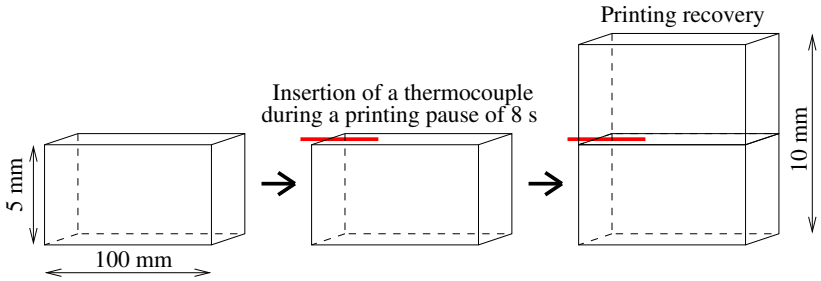

Figure 33: Side view of the three steps of the thermocouple insertion during the wall printing composed by four filaments.

5.1. Thermal behavior of the printed wall

5.1.1. Experimental observations

A wall of ABS with a length L_M and a height H_M set to 10 and 1 cm, respectively, is printed with different printing velocities. The wall width is composed of four polymer strands, meaning that its thickness depends on the printing velocities. The thermal behavior is studied, as a function of the printing conditions, during the printing of the wall. The temperature is recorded using T-type thermocouples introduced during a printing pause of 8 s when the wall height is equal to 5 mm. Figure 33 illustrates the three steps of the printing experiment of the wall building. The insertion of the thermocouple is depicted in the central sketch. The right picture represents the wall at the end of the experiment.

The location of the thermocouple (at one third of L_M) in the inserted layer is illustrated in Figure 34. The arrows depict the printing direction of the nozzle. The same deposition path is reproduced for all tested conditions. For each tested condition, a minimum of five experiments is achieved. An average of all data is then deduced for each set of parameters.

Figure 35 depicts the temperature recording of five experiments at U =4 m/min and V =1 m/min. The temporal origin is defined when the polymer strand is in contact with the thermocouple. Despite uncertainties on the accurate location of the thermocouple, the reproducibility is satisfying. The solid line is the average curve over the five experiments.

The influence of the printing velocity V is studied by measuring the inter-layer tem-

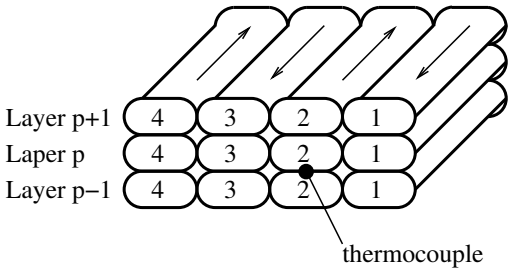

Figure 34: Scheme of the section of a wall where the thermocouple is placed. The arrows depict the printing direction of the nozzle.

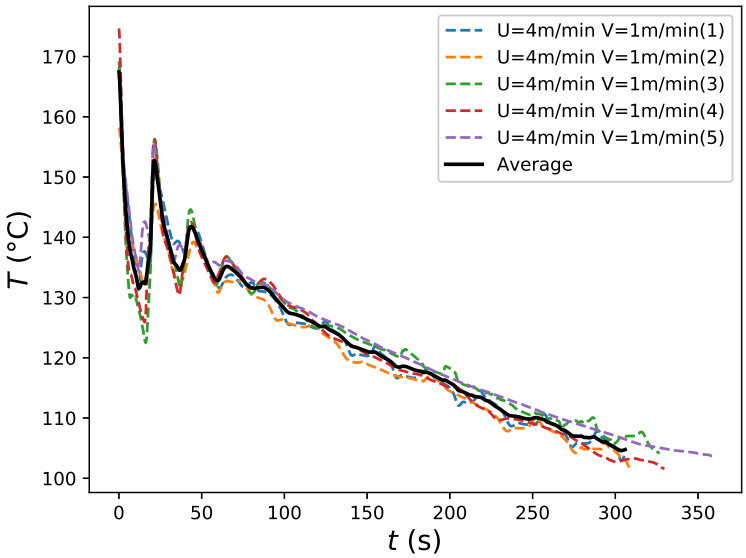

Figure 35: T of the thermocouple as a function of t during the building of a wall. The solid line is the average curve.

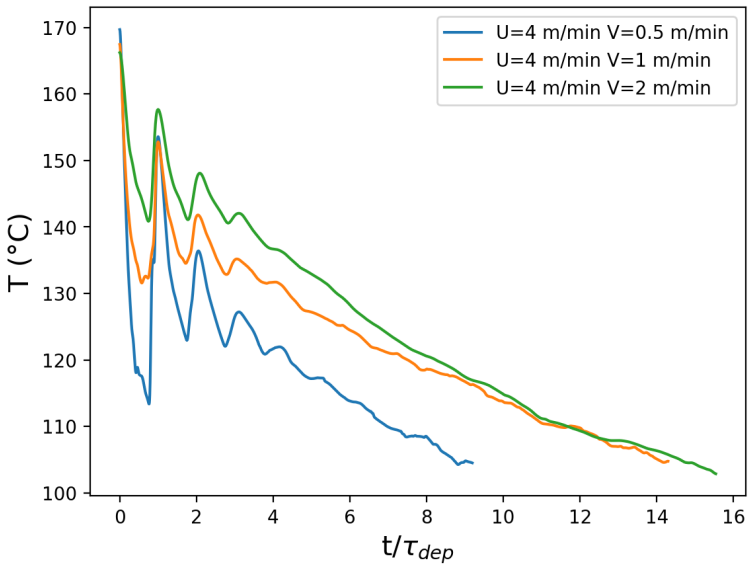

Figure 36: Temperature recorded by the thermocouple as a function of t/τ_{dep} for an extrusion velocity of $4\,\text{m}\,\text{min}^{-1}$ and for three nozzle velocities V equal to 0.5, 1 and $2\,\text{m}\,\text{min}^{-1}$.

perature for three velocities and a constant extrusion velocity U equal to 4 m/min. Figure 36 shows the temperature behavior for the three printing velocities V equal to 0.5, 1 and $2\,\text{m}\,\text{min}^{-1}$. Temperature profiles are plotted as a function of time divided by the period of layer deposition τ_{dep}. This period is equal to 48, 24 and 12 s for V equal to 0.5, 1 and $2\,\text{m}\,\text{min}^{-1}$, respectively.

According to the inter-layer measurements, the printing of a layer p has a major impact on the layers $(p-1)$ and below (Figure 34). Seppala and Migler (2016) have measured the temperature of each layer by Infrared thermography. According to their study, layers below $(p-1)$ are not sufficiently heated to stay above T_g over an extended period of time. In our experiments, Figure 36 shows that the inter-layer temperature stays above Tg during the deposition of multiple layers. The time required to observe an inter-layer temperature below T_g is around 120-265 s. Below this time, adhesion between strands is possible leading to a good welding. When increasing the printing velocity for a constant extrusion velocity the thickness of the deposited layer decreases, but simultaneously the period τ_{dep} decreases too. The amplitude of the two first peaks decreases when the printing velocity increases, but then they become progressively equivalent which is

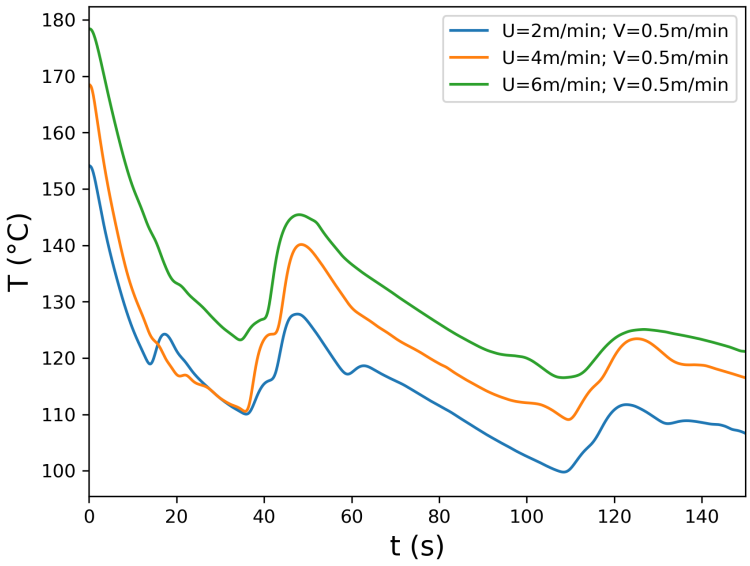

Figure 37: Temperature recorded by the thermocouple as a function of time for a nozzle velocity of $0.5\,\mathrm{m\,min^{-1}}$ and for three extrusion velocities U equal to 2, 4 and $6\,\mathrm{m\,min^{-1}}$.

the result of a subtle balance between the residence time between two successive deposits and the conduction through the deposited strand of varying thickness.

Figure 37 shows the temperature recording at a constant printing velocity V equal to $0.5\,\mathrm{m\,min^{-1}}$ for extrusion velocities U equal to 2, 4 and $6\,\mathrm{m\,min^{-1}}$, respectively. Only the first two periods are recorded for this series of measurements. For U =$2\,\mathrm{m\,min^{-1}}$, a small increase in temperature is noticed when $t \sim 20\,\mathrm{s}$. At this velocity, the strand size is the smallest due to the low extrusion rate. Therefore, the thermocouple is sensitive to the increase of temperature due to the deposition of neighbor strands at the same altitude. A similar event is also seen during the second period of deposition at $t \sim 60\,\mathrm{s}$.

The temperature recorded by the thermocouple increases with the extrusion velocity. This feature seems counter-intuitive since the residence time of the polymer in the extruder decreases with U. Consequently, the heating of the polymer should decrease with U. Peng et al. (2018) observed actually that an increase of the extrusion velocity from 2 to $6\,\mathrm{m\,min^{-1}}$ leads to the decrease of the nozzle exit temperature. This is consistent with Pigeonneau et al. (2020) computations (section 3) who showed a reduction of the temperature on the extruder channel axis for high extrusion velocities (see Figure 5).

However, thermal heterogeneity stays moderate and the average temperature in the exit section of the nozzle remains close to the preset extrusion temperature. Consequently, the variation of temperature observed in Figure 37 is mainly explained by the stored energy $\dot{Q}$ which is proportional to U (Eq. 54). Therefore, the temperature increases with the amount of extruded material.

To understand these, sometimes, counterintuitive temperature recordings, a numerical computation has been developed by Xu et al. (2021).

5.1.2. Numerical predictions

A rectangular domain of width W_M, length L_M and height H_W, similar to the experiments presented in Figure 33, is numerically printed. The polymer is deposited by the introduction of a series of fractions within one layer. The wall width W_M is divided into segments of same size ΔW representing strands of polymer. This means that the cross-section of the deposited strand is idealized as a rectangle. This is consistent with the approximate deposition model proposed in § 4.1.1 but obviously different from the experimental and computed cross-sections (Figure 24 and Figure 25). This means also that the porosity between the deposited stands is neglected. A single strand of length L_M is divided into fractions of length ΔL. Each parallelepipedal fraction of strand (ΔL, ΔW, ΔH) is successively added after a time step dependent on the nozzle velocity V. A single strand line is deposited during a time t_l defined as follows:

$$t_l = \frac{L}{V}. \tag{55}$$

The deposition time of a strand fraction t_f depends on the number of fractions n of a strand defined by

$$t_f = \frac{t_l}{n} = \frac{\Delta L}{V}. \tag{56}$$

After each time step t_f, thermal properties of a volume fraction $\Delta H \Delta W \Delta L$ change from air to polymer. The successive deposition of melted polymer during 3d printing is thus mimicked. The numerical procedure is illustrated in Figure 38.

The temperature field obeys the unsteady heat transfer equation given by:

$$\rho C_p \frac{\partial T}{\partial t} = \boldsymbol{\nabla} \cdot (k \boldsymbol{\nabla} T) + \dot{q}, \tag{57}$$

(a) Deposition of a sub-layer at $t = nt_f$

(b) Deposition of a sub-layer at $t = (n+1)t_f$

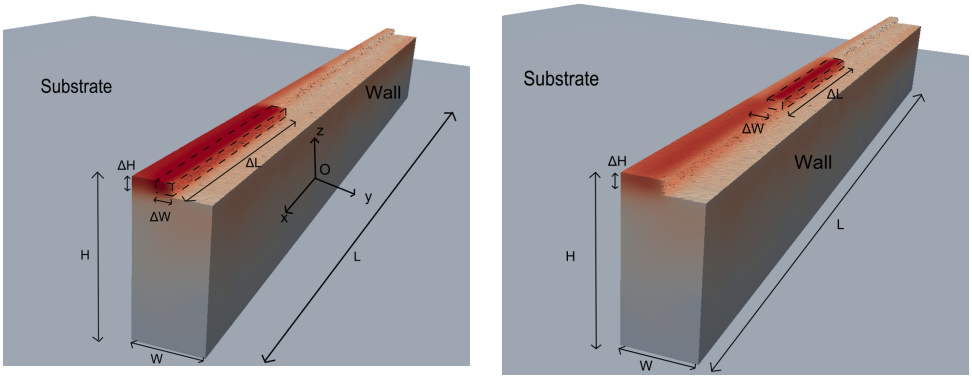

Figure 38: Numerical printing of a wall with two steps of the printing to simulate the FFF process. The origin and the Cartesian coordinate system is depicted in sub-figure 38a.

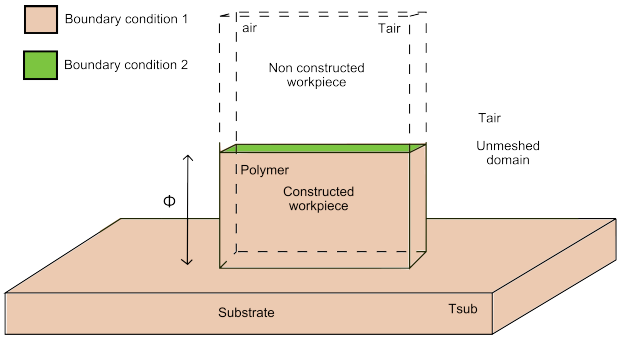

Figure 39: Sketch of the domain with the two kinds of boundary conditions used in numerical computations.

The source term $\dot{q}$ will be detailed below. A perfect contact is assumed between the polymer strands and between the part and the substrate. This is a strong hypothesis as the presence of porosity is practically always seen in FFF. For numerical simplicity the porosity in the part is not taken into account in the meshing. However the thermal conductivity of the polymer is modified to account for the volumetric porosity.

As previously explained, the deposition of polymer fractions is performed by successively changing the properties of the domain from air to polymer at a uniform temperature equal to the extrusion temperature T_{ext}. The substrate temperature is T_{sub}. The air surrounding the wall has a constant temperature T_{air}. Two boundary conditions are

defined to account for the heat transfer with the surrounding air. Along the surface of the solid domain, denoted as boundary condition 1 in Figure 39, a Fourier boundary condition is used:

$$-k\boldsymbol{\nabla}T \cdot \boldsymbol{n} = \mathfrak{h}_{\text{surf}}(T - T_{\text{air}}), \tag{58}$$

with $\boldsymbol{n}$ the unit outward normal, $\mathfrak{h}_{\text{surf}}$ the heat transfer coefficient and T_{air} the air temperature assumed constant.

The convective heat transfer between the top surface of the printing object and the surrounding air has also to be accounted for. This surface is represented as boundary condition 2 in Figure 39. Since this boundary is immersed in the computation domain, the boundary condition is seen as a heat input $\dot{q}$ introduced in equation (57). This sink term is applied in the whole layer in printing written as follows:

$$\dot{q} = \frac{\mathfrak{h}_{\text{top}}(T_{\text{air}} - T)}{\Delta H}, \tag{59}$$

with $\mathfrak{h}_{\text{top}}$ the convective heat transfer coefficient with the surrounding air above the printed object.

In Figure 40, three printing conditions of an ABS polymer, which thermal data are listed in Appendix B, have been considered with different extrusion and printing velocities. In each case the blue line corresponds to the numerical result while the orange line is the temperature recorded experimentally. The glass transition temperature (green line) is also drawn. The successive heating and cooling simulated conditions are in good agreement with experimental measurements.

Nevertheless, the numerical results seem more sensitive to adjacent depositions of new hot filaments than the experimental ones. The temperature increase is numerically observed when deposition of the adjacent strand occurs. The inter-layer reheating due to the deposition of a new layer is strongly reduced once it is covered by more than three layers. After an extended period of time, the steady-state cooling observed experimentally is numerically very well reproduced.

The heat transfer coefficients $\mathfrak{h}_{\text{surf}}$ and $\mathfrak{h}_{\text{top}}$ are set equal to 13 and $8\,\text{Wm}^{-2}\text{K}^{-1}$, respectively to observe a good agreement with experimental results in Figure 40a. These values are significantly lower than the one used in the heat transfer literature devoted to FFF printing. Bellehumeur et al. (2004) have chosen the heat transfer coefficient

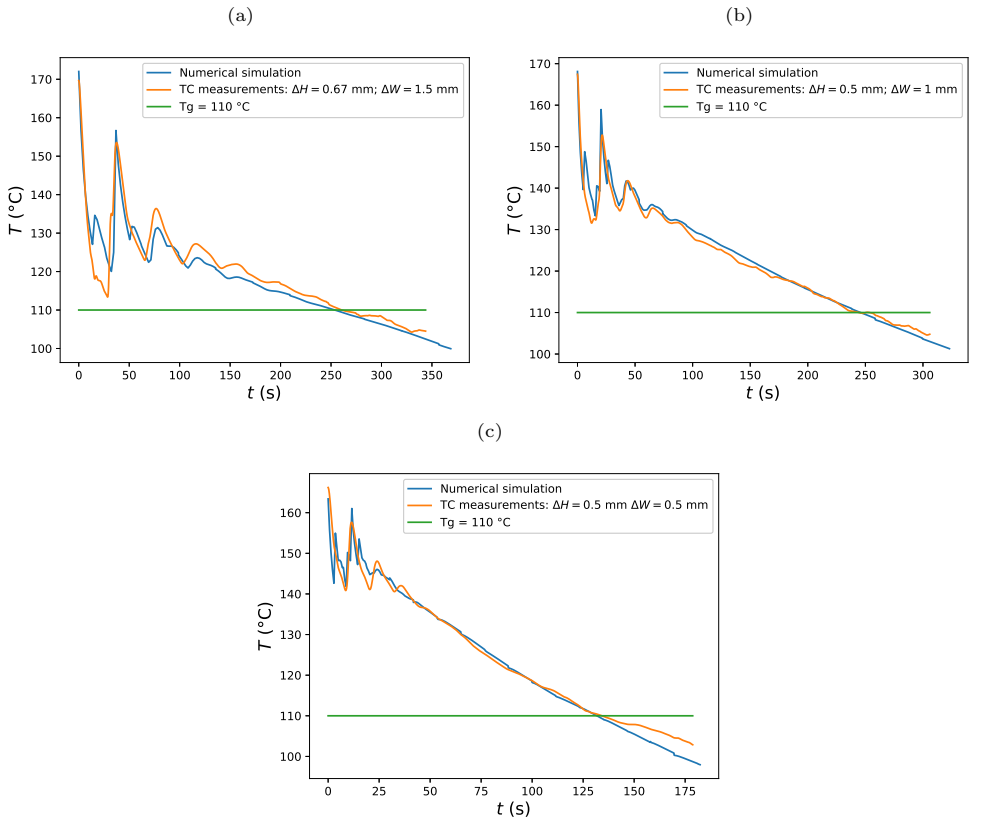

Figure 40: Inter-layer temperature as a function of time. Comparison between numerical and experimental results for (a) U=4.3 m min^{-1} and V=2.14 m min^{-1}, (b) U=4.82 m min^{-1} and V=1.2 m min^{-1} and (c) U=5.36 m min^{-1} and V=0.663 m min^{-1}.

equal to $30\,\mathrm{Wm^{-2}K^{-1}}$ to compute the temperature profile of a single deposited strand for T_{air}=70 °C. To match with their experimental measurements, Costa et al. (2017) set a convective heat transfer coefficient at $62\,\mathrm{Wm^{-2}K^{-1}}$.

Figure 40b and Figure 40c give the inter-layer temperature as a function of time for two other couples of printing conditions. The numerical results have been obtained with the same heat transfer coefficients as in Figure 40a. The maximum temperature of each peak matches very well with the experimental measurements. As previously observed, the strand's computed temperatures are more sensitive to the deposition of adjacent strands.

5.2. Welding between successive strands

Welding between successive printed stands is a key issue for the production of technical parts with relevant mechanical properties. The pressure exerted during the printing of the successive layers will contribute to reduce porosity between the strands, but the interlayer temperature is the prevalent parameter. The situation is different when considering amorphous polymers or semicrystalline polymers. For amorphous polymers welding will be governed by macromole interdiffusion between neighbor strands which is a temperature dependent phenomenon. For semicrystalline polymers, the successive quenching and re-heating of the inter-layer areas between stands, as presented on Figure 40, will induce the development of specific crystalline structures.

5.2.1. Welding of amorphous polymers

At a temperature below the glass transition temperature T_g (represented by a green line on Figure 40) macromolecule diffusion is frozen. Above T_g, the time required for welding is linked to the reptation time of macromolecules t_R (de Gennes, 1971) which depends on the gap between the strands interface temperature and T_g. The welding mechanism has been described by Wool et al. (1989) in Figure 41.

The vertical line represents the contact time between the two polymer layers and the points on each side of this interface are the extremities of the polymer chains. As time goes on the interdiffusion distance χ increases and reaches a maximum value for $t = t_R$.

Yang and Pitchumani (2002) defined a healing rate D_h as the ratio between the interdiffusion length χ at time t to the one obtained at an infinite time. Instead of the

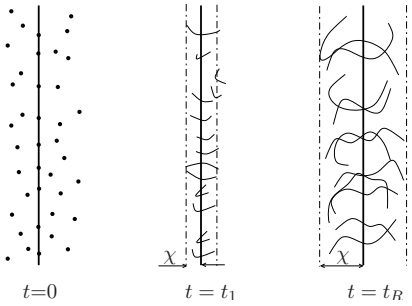

Figure 41: Interdiffusion at the interface between two molten polymer layers according to Wool et al. (1989).

reptation time t_R which has been used by McIlroy and Olmsted (2017), they introduced a welding time t_w which is a function of temperature. The healing rate writes in the isothermal case:

$$D_h(t) = \sqrt[4]{\frac{t}{t_w(T)}}, \tag{60}$$

with

$$t_w(T) = A_h \exp\left[\frac{E}{R}\left(\frac{1}{T} - \frac{1}{T_{\text{ref}}}\right)\right], \tag{61}$$

with E an activation energy, T_{ref} a reference temperature. The pre-factor A_h is a constant which depends on the printed polymer. If the temperature changes over time, which is the situation during printing, the healing rate is generalized as:

$$D_h(t) = \sqrt[4]{\int_0^t \frac{d\tau}{t_w[T(\tau)]}}. \tag{62}$$

Using the numerical method developed by Xu et al. (2021), Xu (2021) printed a more complex ABS part, with both thin and thick walls (Figure 42). He applied equation (62) to determine its healing quality using the data proposed by Ko et al. (2019) for a PC-ABS copolymer which T_g is near the glass transition temperature of ABS (A_h=726 s; E=40.6 kJ mol^{-1}; T_{ref}=230 °C). At the end of printing, healing is better (D_h is higher) in the thick walls of the part than in the thin ones. The thick walls cool more slowly than thin walls and thus the welding quality improves.

5.2.2. Welding of semi-crystalline polymers

Commercial printers for industrial applications increasingly allow the printing of semi-crystalline polymers, particularly high-performance polymers such as PEEK. During

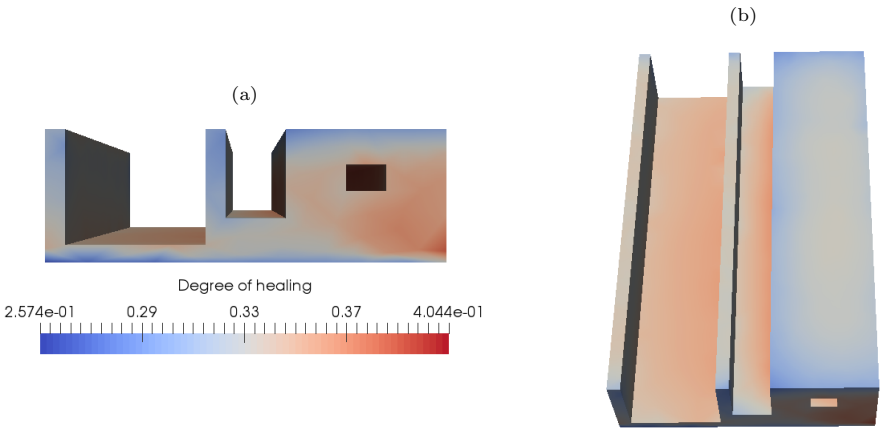

Figure 42: Degree of healing of the object at the end of printing from (a) front view and (b) top view.

strand solidification, crystalline regions act as fillers, reinforcing the material. Crystallinity is a major factor in determining the mechanical properties of printed parts (Kishore et al., 2016). Semi-crystalline polymers can therefore enhance the performance of printed objects. However, solidification of semi-crystalline polymers leads to much greater shrinkage than that observed with amorphous polymers. This can lead to residual stresses and deformation (warpage) of the printed parts. To better understand the effects of crystallization during printing, experimental studies have been carried out using sophisticated measurement systems.

Figure 43 illustrates the shear rate map around the nozzle outlet during the deposition of an ABS filament. The simulation is based on a nozzle diameter of 0.4 mm and a distance between the nozzle and the deposition plane of 0.65 mm, corresponding to a case presented in § 4.2.2. Below the nozzle, shear rates are high. As soon as the strand leaves the area constrained between the bottom of the printhead and the substrate, shear rate decreases sharply and disappears completely away from the printing head.

This allows the deposit to be decomposed into two regions (McIlroy and Graham, 2018): (i) a region under the nozzle with high shear and where the temperature is close to that of the extruder; (ii) and a second region, when the filament is aligned in the flow axis and only in contact with the part previously printed. Here, temperature decreases very rapidly, and the shear rate is zero. To study post-deposition crystallization, Northcutt et al. (2018) developed an experimental setup.

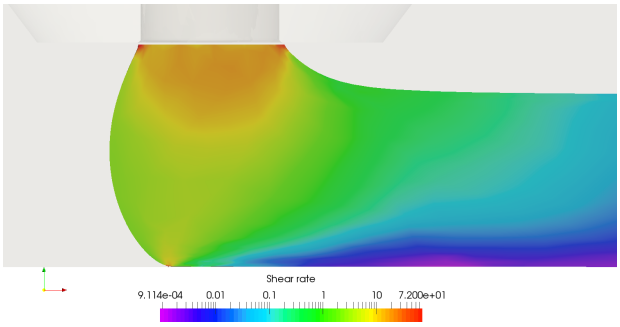

Figure 43: Shear rate field during the deposition of a thread obtained from the numerical computation presented in § 4.2.2.

A fixed printing head deposes a strand on a conveyor belt. A Raman spectrometer is positioned downstream of the printing zone to investigate crystallization in the freshly deposited filament. The study focused on polycaprolactone (PCL) strands with a melting temperature equal to 60 °C. To study the combined influence of temperature and shear rate, the extruder was run at temperatures of 90, 110 and 140 °C, respectively and an extrusion velocity ranging from 25 to 45 mm s^{-1}. Figure 44 plots the time, denoted t_{10}, to achieve 10 % crystallization on the strand top surface as a function of extrusion velocity.

At the highest temperature, crystallization time is only marginally influenced by the velocity. As temperature decreases, crystallization time decreases, and decreases more sharply with increasing extrusion velocity. At high polymer temperatures in the heat block, the strand cools slowly, delaying crystallization. At lower temperatures, crystallization starts earlier in regions where polymer is still subjected to shear rates. The reduction in crystallization time with the increase of U is a signature of flow-induced crystallization.

The polymer extrusion temperature, as well as the ambient air temperature, are key parameters for controlling crystallization kinetics. Spoerk et al. (2018) have studied the effect of the temperature of the printing environment on the crystallization of a polypropylene (PP), specifically developed for FFF 3D printing. Printing takes place in a temperature-controlled chamber, noted T_{ch}. Figure 45 shows two images of printed filaments obtained using a polarized light microscope (Spoerk et al., 2018).

The size of the spherulites is significantly smaller in the interlayer welding zone

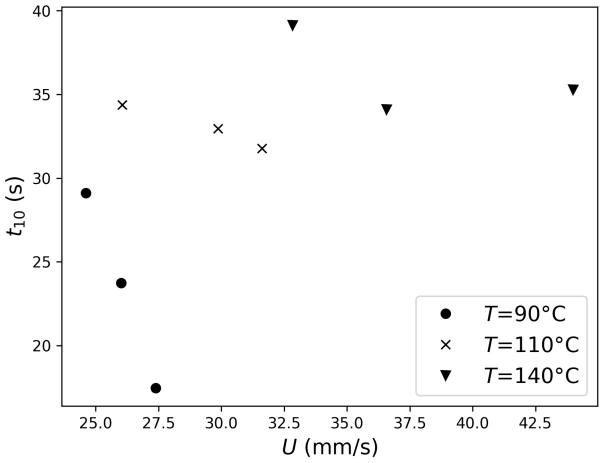

Figure 44: Crystallization time to obtain a crystallization rate of 10 % t_{10} at the strand top surface as a function of the extrusion velocity according to Northcutt et al. (2018).

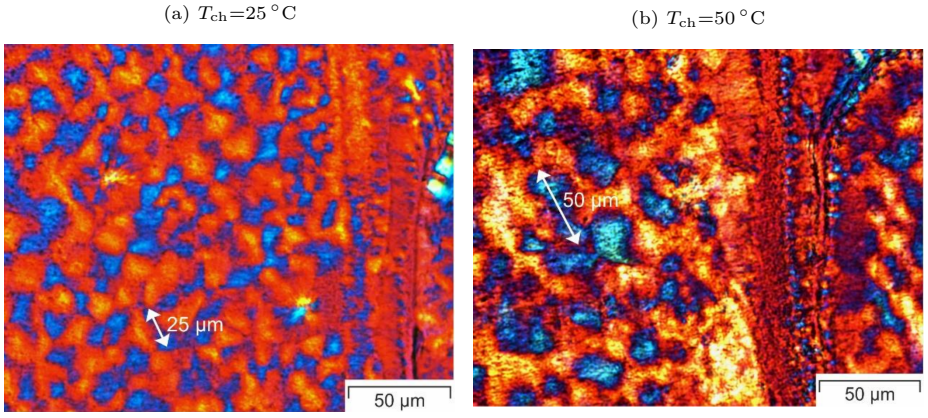

Figure 45: Polarized optical microscopy of Polypropylene strands printed in a chamber at (a) T_{ch}=25 °C and (b) T_{ch}=50 °C from Spoerk et al. (2018, Figure 7(c) and 7(d)) (reproduced under Creative Commons Attribution License and the agreement of the authors).

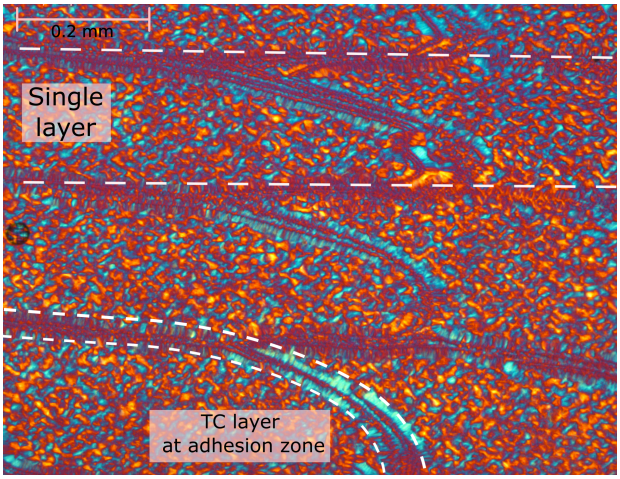

Figure 46: Microstructure of a Polypropylene wall printed at U=2 m min^{-1} and V=1 m min^{-1} achieved by Xu (2021). The transcrystalline layers are referred as TC. The bar scale on the top left of the picture is equal to 0.2 mm.

than within the strands. Otherwise, increasing temperature creates fewer but larger spherulites. Indeed, increasing the chamber temperature causes the deposited strand to be maintained at a temperature close to the temperature of the maximum growth rate of PP spherulites. On the other hand, at temperatures below PP's maximum crystal growth rate, spherulites are smaller but more numerous. Xu (2021) performed similar experiments and observations with another Polypropylene also dedicated to FFF printing, with a crystallization temperature (110 °C) much lower than the usual crystallization temperature of PP. As illustrated in Figure 46, spherulites are again observed in the core of the strands, but now the welding zone is dominantly composed of transcrystalline structures.

For both polypropylene formulations, the interface between strand presents a quite different morphology than the one observed in the core of the strands. The development of small size spherulites or of transcrystalline structures will favor welding and improve the mechanical properties of the printed part.

6. Conclusion

This chapter focuses on the key stages of additive manufacturing using material extrusion process (FFF). The principle of this technology is simple. Although robotization is important in 3D printers, it is necessary to master the successive stages of the process: i) melting/plasticizing in the heating element, ii) depositing the strand, iii) then cooling it and welding it to neighboring strands. A crucial element is the extruder, which ensures the transition from solid to liquid state in a centimetric space. The polymer's residence time in the heat block is just a few seconds. Here again, as in many plastic parts manufacturing processes, shear-thinning behavior of polymers makes it possible to create extrudates with small diameter with moderate efforts.

Thermal studies in the extruder show that filament feed speed plays a crucial role in the heating process and determine the filling force. It is possible to determine a limit extrusion speed to avoid printing head blocking, even if, in common use of an FFF printer, an imposed filling or extrusion speed is not required. The user simply defines the extruder and platen temperatures, the gap between the nozzle base and the substrate and the printing velocity. The filament speed is deduced, but may sometimes lead to blocking phenomena, buckling instabilities between the feeding rollers and the printing head inlet, or to badly melted extrudates.

The shape of the deposited strand is a key point. It depends on the velocity ratio U/V and on the ratio between the nozzle outlet diameter and the gap between the extruder head and the printing surface. As we have seen, when the gap is smaller than the nozzle diameter, the strand has an oblong cross-section. Conversely, when the gap is greater than the nozzle diameter, the crosssection is more elliptical. The size of the deposited strand governs the lateral and vertical displacement of the printing head after the deposition of each layer. Analytical formula for the strand dimensions has been proposed, consistent with experiments as well as with 3D numerical simulations. Otherwise, the pressure induced during the deposition step is very different for a gap smaller or bigger than the nozzle diameter, and this influences the contact between the successive strand layers as well as the importance of porosity.

It is very important to control the cooling of the strands to ensure good adhesion between successive layers. In the case of amorphous polymers, we have seen that the

longer the time spent above the glass transition temperature, the better the adhesion. Opening up 3D printing to technical polymers (in particular semi-crystalline polymers) requires the design of temperature-controlled printers. Such printers already exist and offer promising prospects.

Further development of the filament deposition additive manufacturing process requires, first and foremost, improved melting in the heat block. Otherwise, accounting for the viscoelastic rheological properties of molten polymers is important for better predicting the shape of the extrudate strand as well as the stresses exerted on the substrate. It is a real numerical challenge to capture the free surface of the polymer extrudate which a viscoelastic constitutive equation induces stress singularities at the nozzle exit.

Despite the considerable progress made on the FFF process in recent years, mechanical properties are still considered insufficient, due in particular to the existence of porosities. The demand for parts with good mechanical properties calls for the use of semi-crystalline polymers, for which the printing temperature window is wider than for amorphous polymers. Investigation of the physics specific to semi-crystalline polymers in successive cooling and reheating steps needs to be developed and incorporated in numerical simulation tools.

Although mainly dedicated to polymers, the molten-filament printing process could be applied to other materials. In his original patent, Crump (1992) claimed application to glass. Initial attempts have recently been made to produce chalcogenide glass optical fibers with glass transition temperatures close to those of amorphous polymers Carcreff et al. (2021).

Appendix A. Table of notations

Dimension numbers

Symbol	**Description**
Bi	Biot number
Br	Brinkmann number
Ca	Capillary number
Pe	Péclet number

Re	Reynolds number
Wi	Weissenberg number

Roman Characters

Symbol	**Description**	**Unit**
$\mathcal{A}$	Area of the cross-section of a deposited strand	m^2
A_h	prefactor of the welding time between two filaments	s
a	parameter of the Carreau-Yasuda's law controlling the transition between the Newtonian and pseudo-plastic regimes	$-$
a_T	temperature shift factor	$-$
C_p	specific heat capacity at constant pressure	$\mathrm{J\,kg^{-1}\,K^{-1}}$
D	Barrel diameter of the extruder	m
D_f	Filament diameter	m
D_h	Healing degree	$-$
d	Nozzle capillary diameter	m
d_Γ	Euclidean distance from the interface $\Gamma(t)$	m
E	Activation energy of the welding time	$\mathrm{J\,mol^{-1}}$
E_a	Activation energy of the viscosity	$\mathrm{J\,mol^{-1}}$
e	Gap between the printing plane and the tip of the nozzle	m
e_{air}	Gap between the filament and the extruder barrel wall	m
F	Feeding force applied on the filament	N
H	Height of the deposited strand	m
$\mathcal{H}$	Generalized Heaviside function	$-$
H_M	Height of the printed wall	m
$\mathfrak{h}_{\mathrm{air}}$	Heat transfer between the strand, the printed wall, and the surrounding air	$\mathrm{WK^{-1}m^{-2}}$
$\mathfrak{h}_{\mathrm{ext}}$	Heat transfer coefficient between the extruder and the filament	$\mathrm{WK^{-1}m^{-2}}$

$\mathfrak{h}_{\text{sub}}$	Heat transfer coefficient between the printed strand and the printing plane, the substrate	$\text{WK}^{-1}\text{m}^{-2}$
$\mathfrak{h}_{\text{surf}}$	Heat transfer coefficient at the lateral surface of the printed wall	$\text{WK}^{-1}\text{m}^{-2}$
$\mathfrak{h}_{\text{top}}$	Heat transfer coefficient at the upper surface of the printed wall	$\text{WK}^{-1}\text{m}^{-2}$
K	Polymer consistency	Pas^n
k	Thermal conductivity of polymer	$\text{WK}^{-1}\text{m}^{-1}$
k_{air}	Thermal conductivity of air	$\text{WK}^{-1}\text{m}^{-1}$
L	Length of heat block of the extruder	m
L_M	Length of the printed wall	m
L_{T_g}	Melting distance in the heat block	m
l	length of the capillary channel in the nozzle	m
l_f	spreading distance in front of the extruder	m
n	Shear thinning index	–
$\mathcal{P}$	perimeter of the cross-section of a strand	m
P	pressure	Pa, –
P_0	pressure at nozzle exit in confined flow situation	Pa
$\dot{Q}$	Stored energy in the deposited strand	W
q	Volumic flow rate pet unit width	m^2s^{-1}
$\dot{q}$	Source term in the printing of a wall	Wm^{-3}
R	ideal gas constant [8.314]	$\text{J mol}^{-1}\,\text{K}^{-1}$
r	Nozzle capillary radius	m
r_e	Nozzle external radius	m
T	Temperature	K, °C
T_{air}	Ambient temperature	K, °C
T_{ch}	Controlled temperature of a printing chamber	K, °C
T_{ext}	Controlled temperature of heat block	K, °C
T_{g}	Temperature of the glass transition	K, °C
T_{ref}	Reference temperature	K, °C

T_{sub}	Temperature of the building platform, of the substrate	K, °C
T_0	Filament temperature at the heat block inlet	K, °C
t	time	s
t_R	reptation time	s
t_w	welding time between two strands	s
U	Extrusion velocity at nozzle exit	$\mathrm{m\,s^{-1}}$
U_{in}	Filament velocity at extruder inlet	$\mathrm{m\,s^{-1}}$
U_{lim}	Maximum velocity of the filament in the heat block	$\mathrm{m\,s^{-1}}$
V	Printing velocity	$\mathrm{m\,s^{-1}}$
x	Cartesian or axial coordinate	m
W	Width of the deposited strand	m
W_M	Width of the printed wall	m
y	Cartesian coordinate	m
z	Cartesian coordinate	m

Greeks characters

Symbol	**Description**	**Unit**
α	Dimensionless number equal to $dU/(eV)$	–
β	Parameter of the mean temperature in the cooling step of a strand	–
γ	Surface tension between the polymer strand and the surrounding air	$\mathrm{N\,m^{-1}}$
$\dot{\gamma}$	Generalized shear rate	$\mathrm{s^{-1}}$
$\dot{\boldsymbol{\varepsilon}}$	Rate-of-strain tensor	$\mathrm{s^{-1}}$
η	Dynamic viscosity	Pa s, –
η_0	Dynamic viscosity on the Newtonian plateau	Pa s
θ	Dimensionless temperature	–
$\overline{\theta}$	Dimensionless average temperature over the cross-section of the deposited strand	–
κ_Γ	Free surface curvature	$\mathrm{m^{-1}}$
λ	Relaxation time in the Carreau-Yasuda rheology law	s

ρ	density	kgm^{-3}
τ_{dep}	Period of layer deposition during wall printing	s
φ	Level-set function	m
ϕ	Half angle of the convergent of the nozzle	rad
χ	Thickness of the inter-diffusion layer between two strands	m
χ_{air}	Portion of the strand perimeter in contact with air	–
χ_{sub}	Portion of the strand perimeter in contact with the substrate	–

Appendix B. Rheology and thermal data of printed polymers

Table B.4: Mechanical and thermal properties of ABS and PC polymers.

η_0	λ	a	n	E_a	T_{ref}	ρ	C_p	k	T_g
Pa s	s	–	–	$\mathrm{kJ\,mol^{-1}}$	°C	$\mathrm{kg/m^3}$	$\mathrm{J\,kg^{-1}\,K^{-1}}$	$\mathrm{W\,m^{-1}\,K^{-1}}$	°C
ABS									
3.04×10^3	3.2×10^{-3}	0.6	0.27	115	220	1150	2100	0.21	110
PC									
5.3×10^2	1.2×10^{-4}	1	0.31	100	320	1200	1250	0.21	150

References

Agassant, J.F., Avenas, P., Carreau, P.J., Vergnes, B., Vincent, M., 2017. Polymer processing: principles and modeling. Carl Hanser Verlag GmbH Co. doi:10.3139/9781569906064.

Agassant, J.F., Pigeonneau, F., Sardo, L., Vincent, M., 2019. Flow analysis of the polymer spreading during extrusion additive manufacturing. Addit. Manuf. 29, 100794. doi:10.1016/j.addma.2019.100794.

Bejan, A., 2013. Convection heat transfer. Third ed., John Wiley & Sons, Hoboken, New Jersey. doi:10.1002/9781118671627.

Bell, C., 2015. 3D Printing with Delta Printers. Apress.

Bellehumeur, C., Li, L., Sun, Q., Gu, P., 2004. Modeling of bond formation between polymer filaments in the fused deposition modeling process. J. Manuf. Processes 6, 170–178. doi:10.1016/s1526-6125(04)70071-7.

Bellini, A., Güçeri, S., Bertoldi, M., 2004. Liquefier dynamics in fused deposition. J. Manuf. Sci. Eng. 126, 237–246. doi:10.1115/1.1688377.

Bird, R.B., Armstrong, R.C., Hassager, O., 1987. Dynamics of polymeric liquids: Vol. 1 Fluid mechanics. 2nd ed., Wiley-Interscience.

Bonito, A., Guermond, J.L., Lee, S., 2016. Numerical simulations of bouncing jets. Int. J. Numer. Meth. Fluids 80, 53–75. doi:10.1002/fld.4071, arXiv:https://onlinelibrary.wiley.com/doi/pdf/10.1002/fld.4071.

Brackbill, J.U., Kothe, D.B., Zemach, C., 1992. A continuum method for modeling surface tension. J. Comput. Phys. 100, 335 – 354. doi:10.1016/0021-9991(92)90240-Y.

Brooks, A.N., Hughes, T.J.R., 1982. Streamline upwind/petrov-galerkin formulations for convection dominated flows with particular emphasis on the incompressible navier-stokes equations. Comput. Methods Appl. Mech. Engrg. 32, 199–259. doi:10.1016/0045-7825(82)90071-8.

Carcreff, J., Cheviré, F., Lebullenger, R., Gautier, A., Chahal, R., Adam, J.L., Calvez, L., Brilland, L., Galdo, E., Le Coq, D., Renversez, G., Troles, J., 2021. Investigation on chalcogenide glass additive manufacturing for shaping mid-infrared optical components and microstructured optical fibers. Crystals 11, 228. doi:10.3390/cryst11030228.

Carreau, P.J., 1972. Rheological equations from molecular network theories. Trans. Soc. Rheol. 16, 99–127. doi:10.1122/1.549276.

Costa, S.F., Duarte, F.M., Covas, J.A., 2017. Estimation of filament temperature and adhesion development in fused deposition techniques. J. Mater. Process. Technol. 245, 167–179. doi:10.1016/j.jmatprotec.2017.02.026.

Crump, S.S., 1992. Apparatus and method for creating three-dimensional objects. US Patent 5,121,329.

Das, A., McIlroy, C., Bortner, M.J., 2020. Advances in modeling transport phenomena in material-extrusion additive manufacturing: Coupling momentum, heat, and mass transfer. Prog. Addit. Manuf. 6, 3–17. doi:10.1007/s40964-020-00137-3.

Datsiou, K.C., Saleh, E., Spirrett, F., Goodridge, R., Ashcroft, I., Eustice, D., 2019. Additive manufacturing of glass with laser powder bed fusion. J. Am. Ceram. Soc. 102, 4410–4414. doi:10.1111/jace.16440.

de Gennes, P.G., 1971. Reptation of a polymer chain in the presence of fixed obstacles. J. Chem. Phys. 55, 572–579. doi:10.1063/1.1675789.

Di Pietro, D.A., Ern, A., 2012. Mathematical aspects of discontinuous Galerkin methods. Springer-Verlag, Heidelberg.

E3D-online, 2021. E3d help centre. https://e3d-online.zendesk.com/hc/en-us.

Ern, A., Guermond, J.L., 2004. Theory and practice of finite elements. volume 159. Springer Science & Business Media.

Ern, A., Guermond, J.L., 2021. Finite Elements II: Galerkin Approximation, Elliptic and Mixed PDEs. Springer International Publishing. doi:10.1007/978-3-030-56923-5.

Fico, D., Rizzo, D., Casciaro, R., Esposito Corcione, C., 2022. A review of polymer-based materials for fused filament fabrication (FFF): Focus on sustainability and recycled materials. Polymers 14, 465. doi:10.3390/polym14030465.

Fourier, J., 1822. Théorie analytique de la chaleur. Firmin Didot, Péres et fils.

Gavis, J., Modan, M., 1967. Expansion and contraction of jets of Newtonian liquids in air: Effect of tube length. Phys. Fluids 10, 487–497. doi:10.1063/1.1762142.

Gibson, I., Rosen, D., Stucker, B., 2015. Additive Manufacturing Technologies: 3D Printing, Rapid Prototyping, and Direct Digital Manufacturing. 2nd ed., Springer. doi:10.1007/978-1-4939-2113-3.

Go, J., Schiffres, S.N., Stevens, A.G., Hart, A.J., 2017. Rate limits of additive manufacturing by fused filament fabrication and guidelines for high-throughput system design. Addit. Manuf. 16, 1–11. doi:10.1016/j.addma.2017.03.007.

Groß, S., Reusken, A., 2011. Numerical methods for two-phase incompressible flows. volume 40 of *Springer series in computational mathematics*. Springer-Verlag, Berlin. doi:10.1007/978-3-642-19686-7.

Halidi, S.N.A.M., Abdullah, J., 2012. Moisture effects on the ABS used for fused deposition modeling rapid prototyping machine, in: IEEE Symposium on Humanities, Science and Engineering Research, pp. 839–843. doi:10.1109/SHUSER.2012.6268999.

Hebda, M., McIlroy, C., Whiteside, B., Caton-Rose, F., Coates, P., 2019. A method for predicting geometric characteristics of polymer deposition during fused-filament-fabrication. Addit. Manuf. 27, 99 – 108. doi:10.1016/j.addma.2019.02.013.

Hirt, C.W., Nichols, B.D., 1981. Volume of fluid (VoF) method for the dynamics of free boundaries. J. Comput. Phys. 39, 201–226. doi:10.1016/0021-9991(81)90145-5.

Hong, Y., Mrinal, M., Phan, H.S., Tran, V.D., Liu, X., Luo, C., 2022. In-situ observation of the extrusion processes of acrylonitrile butadiene styrene and polylactic acid for material extrusion additive manufacturing. Addit. Manuf. 49, 102507. doi:10.1016/j.addma.2021.102507.

ISO/ASTM, 2021. Additive manufacturing — General principles — Fundamentals and vocabulary. techreport ISO/ASTM 52900. International Organization for Standardization. doi:10.3403/30448424.

Jannoun, G., Hachem, E., Veysset, J., Coupez, T., 2015. Anisotropic meshing with time-stepping control for unsteady convection-dominated problems. Appl. Math. Modell. 39, 1899 – 1916. doi:10.1016/j.apm.2014.10.005.

Jones, R., Haufe, P., Sells, E., Iravani, P., Olliver, V., Palmer, C., Bowyer, A., 2011. RepRap – the replicating rapid prototyper. Robotica 29, 177–191. doi:10.1017/S026357471000069X.

Kataoka, I., 1986. Local instant formulation of two-phase flow. Int. J. Multiphase flow 12, 745–758. doi:10.1016/0301-9322(86)90049-2.

Kishore, V., Chen, X., Ajinjeru, C., Hassen, A.A., Lindahl, J., Failla, J., Kunc, V., Duty, C., 2016. Additive manufacturing of high performance semicrystalline thermoplastics and their composites, in: International Solid Freeform Fabrication Symposium, University of Texas at Austin. pp. 906–915.

Ko, Y.S., Herrmann, D., Tolar, O., Elspass, W.J., Brändli, C., 2019. Improving the filament weld-strength of fused filament fabrication products through improved interdiffusion. Addit. Manuf. 29, 100815. doi:10.1016/j.addma.2019.100815.

Mackay, M.E., Swain, Z.R., Banbury, C.R., Phan, D.D., Edwards, D.A., 2017. The performance of the hot end in a plasticating 3D printer. J. Rheol. 61, 229–236. doi:10.1122/1.4973852.

Marion, S., Sardo, L., Joffre, T., Pigeonneau, F., 2023. First steps of the melting of an amorphous

polymer through a hot-end in fused filament fabrication. Addif. Manuf. 65, 103435. doi:10.1016/j.addma.2023.103435.

McIlroy, C., Graham, R.S., 2018. Modelling flow-enhanced crystallisation during fused filament fabrication of semi-crystalline polymer melts. Addit. Manuf. 24, 323–340. doi:10.1016/j.addma.2018.10.018.

McIlroy, C., Olmsted, P.D., 2017. Disentanglement effects on welding behaviour of polymer melts during the fused-filament-fabrication method for additive manufacturing. Polymer 123, 376–391. doi:10.1016/j.polymer.2017.06.051.

Nienhaus, V., Smith, K., Spiehl, D., Dörsam, E., 2019. Investigations on nozzle geometry in fused filament fabrication. Addit. Manuf. 28, 711–718. doi:10.1016/j.addma.2019.06.019.

Northcutt, L.A., Orski, S.V., Migler, K.B., Kotula, A.P., 2018. Effect of processing conditions on crystallization kinetics during materials extrusion additive manufacturing. Polymer 154, 182–187. doi:10.1016/j.polymer.2018.09.018.

Osswald, T.A., Puentes, J., Kattinger, J., 2018. Fused filament fabrication melting model. Addit. Manuf. 22, 51–59. doi:10.1016/j.addma.2018.04.030.

Peng, F., Vogt, B.D., Cakmak, M., 2018. Complex flow and temperature history during melt extrusion in material extrusion additive manufacturing. Addit. Manuf. 22, 197 – 206. doi:10.1016/j.addma.2018.05.015.

Pigeonneau, F., Xu, D., Vincent, M., Agassant, J.F., 2020. Heating and flow computations of an amorphous polymer in the liquefier of a material extrusion 3D printer. Addit. Manuf. 32, 101001. doi:10.1016/j.addma.2019.101001.

Ravoori, D., Lowery, C., Prajapati, H., Jain, A., 2019. Experimental and theoretical investigation of heat transfer in platform bed during polymer extrusion based additive manufacturing. Polym. Test. 73, 439–446. doi:10.1016/j.polymertesting.2018.11.025.

Saramito, P., 2020. Efficient C++ finite element computing with Rheolef. CNRS-CCSD ed. http://hal.archives-ouvertes.fr/cel-00573970.

Seppala, J.E., Migler, K.D., 2016. Infrared thermography of welding zones produced by polymer extrusion additive manufacturing. Addit. Manuf. 12, 71–76. doi:10.1016/j.addma.2016.06.007.

Serdeczny, M.P., Comminal, R., Mollah, M.T., Pedersen, D.B., Spangenberg, J., 2020a. Numerical modeling of the polymer flow through the hot-end in filament-based material extrusion additive manufacturing. Addit. Manuf. 36, 101454. doi:10.1016/j.addma.2020.101454.

Serdeczny, M.P., Comminal, R., Pedersen, D.B., Spangenberg, J., 2018. Experimental validation of a numerical model for the strand shape in material extrusion additive manufacturing. Addit. Manuf. 24, 145–153. doi:10.1016/j.addma.2018.09.022.

Serdeczny, M.P., Comminal, R., Pedersen, D.B., Spangenberg, J., 2020b. Experimental and analytical study of the polymer melt flow through the hot-end in material extrusion additive manufacturing. Addit. Manuf. 32, 100997. doi:10.1016/j.addma.2019.100997.

Sethian, J.A., 1999. Level set methods and fast marching methods. Evolving interfaces in computational geometry, fluid mechanics, computer vision, and materials science. Cambridge University Press, Cambridge.

Sethian, J.A., Smereka, P., 2003. Level set methods for fluid interfaces. Annu. Rev. Fluid Mech. 35, 341–371.

Shah, R.K., London, A.L., 1978. Laminar flow forced convection in ducts. A Source book for compact heat exchanger analytical data. Academic Press, New York.

Silva, L., Valette, R., Laure, P., Coupez, T., 2012. A new three-dimensional mixed finite element for direct numerical simulation of compressible viscoelastic flows with moving free surfaces. Int. J. Mater. Form. 5, 55–72. doi:10.1007/s12289-011-1030-2.

Sneddon, I.N., 1957. Elements of partial differential equations. McGraw-Hill.

Spoerk, M., Arbeiter, F., Raguž, I., Weingrill, G., Fischinger, T., Traxler, G., Schuschnigg, S., Cardon, L., Holzer, C., 2018. Polypropylene filled with glass spheres in extrusion-based additive manufacturing: Effect of filler size and printing chamber temperature. Macromol. Mater. Eng. 303, 1800179. doi:10.1002/mame.201800179.

Süli, E., Mayers, D.F., 2003. An Introduction to Numerical Analysis. Cambridge University Press, Cambridge (UK). doi:10.1017/cbo9780511801181.

Thomas, J.P., Rodríguez, J.F., 2000. Modeling the fracture strength between fused-deposition extruded roads 16, in: 2000 International Solid Freeform Fabrication Symposium, pp. 16–23.

Turner, B.N., Gold, S.A., 2015. A review of melt extrusion additive manufacturing processes: II. Materials, dimensional accuracy, and surface roughness. Rapid Prototyping J. 21, 250–261. doi:10.1108/RPJ-02-2013-0017.

Turner, B.N., Strong, R., Gold, S.A., 2014. A review of melt extrusion additive manufacturing processes: I. Process design and modeling. Rapid Prototyping J. 20, 192–204. doi:10.1108/rpj-01-2013-0012.

Ville, L., Silva, L., Coupez, T., 2011. Convected level set method for the numerical simulation of fluid buckling. Int. J. Numer. Methods Fluids 66, 324–344. doi:10.1002/fld.2259.

Wool, R.P., Yuan, B.L., McGarel, O.J., 1989. Welding of polymer interfaces. Polym. Eng. Sci. 29, 1340–1367. doi:10.1002/pen.760291906.

Xu, D., 2021. Thermomechanical analysis of the Fused Filament Fabrication process: Experimental and numerical investigations. phdthesis. Mines Paris – PSL University. URL: https://pastel.archives-ouvertes.fr/tel-03652351.

Xu, D., Agassant, J.F., Pigeonneau, F., 2022. Dimensions of the deposited strand in the material extrusion process: Experimental and numerical investigations. Addit. Manuf. 59, 103107. doi:10.1016/j.addma.2022.103107.

Xu, D., Zhang, Y., Pigeonneau, F., 2021. Thermal analysis of the fused filament fabrication printing process: Experimental and numerical investigations. Int. J. Mater. Form. 14, 763–776. doi:10.1007/s12289-020-01591-8.

Yang, F., Pitchumani, R., 2002. Healing of thermoplastic polymers at an interface under nonisothermal conditions. Macromolecules 35, 3213–3224. doi:10.1021/ma010858o.